Nonlinear Dyn (2024) 112:6813–6845
https://doi.org/10.1007/s11071-024-09298-0

ORIGINAL PAPER

A nonlinear numerical scheme to investigate the influence of geometric nonlinearity on post-flutter responses of bridges

Kai Li · Yan Han · C. S. Cai · Weiwei Zhang · Jun Song · Hubin Yan

Received: 27 November 2022 / Accepted: 6 January 2024 / Published online: 7 March 2024

Abstract The present study aims to investigate the influence of geometric nonlinearity on post-flutter responses by developing a full-mode coupled nonlinear flutter analysis method (frequency-domain method) and a time-dependent nonlinear analysis scheme (time-domain method). This approach integrates the three-dimensional (3D) nonlinear finite element model and nonlinear self-excited force described by amplitude-dependent rational functions (RFs). By comparing post-flutter responses obtained from frequency-domain and time-domain methods, not only the influence of geometric nonlinearity on post-flutter responses is quantified, but also the underlying physical mechanism is revealed. The results show that the geometric nonlinear effect will become more significant with the increase of the amplitude and thus will induce a super-harmonic resonance behavior. The behavior is mainly characterized by the higher harmonic frequencies vibrations with higher-order mode shapes involved in the vertical and torsional displacement responses. Meanwhile, the larger the vibration amplitude, the more significant the super-harmonic resonance behavior. Besides, the geometric nonlinear effect will also cause a significant uplifting of the bridge deck in the vertical direction during 3D nonlinear flutter process. The main physical mechanism for the reduction in the amplitude of post-flutter response (dominated by the vibration with fundamental harmonic frequency) after considering the geometric nonlinear behavior is that the vibrations with higher harmonic frequencies play a role of absorbing energy and reducing vibration (similar to tuned mass damper effect) for the vibration with fundamental harmonic frequency. For the long-span suspension bridge with a main span of 1650 m studied in this study, the geometric nonlinear effect may need to be considered when the torsional amplitude at mid-span is only greater than 1.5°.

Keywords 3D nonlinear flutter analysis · Time-dependent nonlinear self-excited force model · Geometric nonlinearity · Long-span bridge · Full-mode nonlinear flutter analysis

K. Li · Y. Han (✉) · J. Song · H. Yan
School of Civil Engineering, Changsha University of Science and Technology, 960, 2nd Section, Wanjiali South Road, Changsha 410114, Hunan, China
e-mail: ce_hanyan@163.com

K. Li
e-mail: 1012056203@qq.com

K. Li · W. Zhang
School of Aeronautics, Northwestern Polytechnical University, Xi'an 710072, China
e-mail: aeroelastic@nwpu.edu.cn

C. S. Cai
Department of Bridge Engineering, School of Transportation, Southeast University, Nanjing 211189, China
e-mail: cscai@seu.edu.cn

1 Introduction

After decades of development, linear flutter analysis frameworks have achieved significant progress. On the one hand, by adopting closed-form solutions of bimodal coupled flutter [1, 2] or the step-by-step flutter analysis method [3–6], the mechanisms of flutter for various bridge decks have been further investigated. On the other hand, multimode and full-mode coupled flutter analysis frameworks were developed by considering three-dimensional (3D) aerodynamic effects, and thus, the critical wind speed could be calculated more accurately since both the negative and positive contributions from other modes were considered [7–13]. In the classic linear flutter framework, the self-excited forces are generally modeled as linear functions of vibration velocity and displacement [14]. Accordingly, the vibration of structure is assumed to go unbounded beyond a critical speed.

However, due to the existence of the aeroelastic nonlinearity, extensive numerical and experimental studies [14–19] shown that the flutter derivatives (FDs) of bridge decks (especially for bluff bridge decks) are amplitude-dependent. Besides, it was found by many researchers that flutter vibrations of most bluff bridges exhibit a self-limiting behavior and become limit cycle oscillations (LCOs) beyond the critical speed [20–29]. For relatively bluff sections, such as edge-girders and H-shaped sections, a torsional LCO coupled with a very slight vertical DOF was usually observed [20–22]. While for relatively flat sections, such as flat closed-box sections, thin rectangular plates and truss bridge decks, a vertical–torsional coupled LCO in the torsional mode was usually observed [24–29]. Additionally, it was also found that the amplitudes of LCOs for some bridge decks are strongly affected by wind speed paths or initial conditions [24, 29–31]. The above studies essentially reveal the nonlinear characteristics of aerodynamic forces, which indicates that linear flutter theory is no longer applicable to the analysis of the “soft” flutter (or called as LCO-type flutter).

Nowadays, the costs of construction and design of super long-span bridges have increased dramatically based on the framework of classic linear flutter, which thus has restricted the development trend of bridges to a longer span [29]. In reality, long-span bridges are flexible and their vibration with large amplitude belongs to a typical problem of “large deformation but with small strain”. Therefore, in order to fully exploit the wind-resistant potentialities and reduce the design requirements and difficulties of super long-span bridges, vibrations with acceptable stable amplitudes should be allowed for LCO type of flutter in the future wind-resistant design. However, accurately predicting nonlinear flutter responses (displacement, acceleration, stress, etc.) is a prerequisite for the determination of the acceptable maximum amplitude and the establishment of the future fortification criteria against flutter based on the nonlinear flutter theory (also known as performance-based fortification criteria against nonlinear flutter [36]). To this end, many researchers modeled mathematically nonlinear aeroelastic self-excited forces of typical bridge decks to have a reasonable prediction on nonlinear flutter amplitudes [32–37]. Gao et al. [22] established a single-degree-of-freedom (SDOF) torsional nonlinear self-excited force model for a twin-side-girder bridge deck based on the measured aerodynamic force. Based on the measured displacement from free vibrations of a streamlined section, Zhang et al. [32] also developed a SDOF nonlinear self-excited force model. However, these SDOF models ignored the coupling effect from the vertical DOF. Recently, Gao et al. [33] and Wu et al. [30] proposed 2DOF nonlinear self-excited force models for a streamlined section and a double-deck truss girder section, respectively. Li [34] further proposed a general modeling framework, including multiple nonlinear effects from mechanical nonlinearity, non-wind-induced aerodynamic nonlinearity, and wind-induced aerodynamic nonlinearity, for vertical–torsional coupled nonlinear flutter. This modeling framework was further verified by section model tests of a truss-girder deck with large amplitude vibrations. However, 3D effects in terms of the variation of self-excited forces along the bridge’s span were not considered in the above studies. Based on the nonlinear aerodynamic force model in terms of amplitude-dependent FDs, 3D nonlinear flutter analysis for long-span bridges with a streamlined section and a double-deck truss girder section were conducted by Wang et al. [35] and Wu et al. [28], respectively. In their analysis, the 3D effects in terms of spatial variation of the self-excited forces were considered, but only the fundamental torsional and vertical modes can be included. For this, one of the purposes of this study is to establish a nonlinear flutter analysis framework in which the full-mode coupling effect can be taken into account.

The aforementioned nonlinear self-excited force models are all in hybrid expressions in the time and frequency domains, and they can only be analyzed in the frequency domain, which means structural nonlinearities cannot be considered. To this end, many attempts have been made to express the nonlinear effects of wind–structure interactions for long-span bridges in the time domain [38–48]. Wu and Kareem [39, 40] proposed a nonlinear convolution approach based on Volterra theory to describe linear and nonlinear aerodynamic forces of long-span bridges, but its application is currently limited due to the challenge of identifying higher-order Volterra kernels. Zhang [38] tried an integral-type model to simulate the aerodynamic nonlinearity. Liu [41] and Zhou et al. [42] also attempted a nonlinear aerodynamic force model based on nonlinear differential equations to capture the nonlinear and unsteady aerodynamic effects resulting from various wind velocities and structural vibration amplitudes. However, not only the number of parameters needs to be identified was enormous but also the identification of them needs adopting CFD simulations. Besides, some black-box models [43–48] based on different neural network architectures were adopted to describe nonlinear and unsteady aerodynamic force on bridge decks or airfoils with the rapid development of artificial intelligence technology. However, the generalization of these models needs to be further verified and the interpretability of them needs to be further improved. From a practical point of view, a time-dependent nonlinear self-excited force model whose parameters can be estimated by simple wind-tunnel tests still needs to be investigated, which is the second purpose of this study. Besides, the influence of geometric nonlinearity on post-flutter responses needs to be further quantified and analyzed, which is the ultimate purpose of this study.

In this study, based on amplitude-dependent FDs extracted from free vibration wind tunnel tests, a full-mode nonlinear flutter analysis framework in the frequency domain aiming at a more accurate prediction of the 3D post-flutter responses by taking the full-mode aerodynamic coupling effects into account was proposed and a corresponding iterative algorithm was developed. Subsequently, because the geometric nonlinearity effect cannot be considered in the frequency-domain analysis method, a time-dependent nonlinear unsteady self-excited force model described by amplitude-dependent RFs was established. Finally, an integrated nonlinear numerical scheme integrating the time-dependent nonlinear self-excited force and 3D nonlinear finite element model in the time domain was developed, with which a more accurate post-flutter responses under the coupling effects of multiple nonlinearities (e.g., aerodynamic nonlinearity and structural nonlinearity) can be obtained. Furthermore, by comparing post-flutter responses obtained from the frequency-domain and time-domain methods, not only the influence of geometric nonlinearity on the post-flutter is quantified, but also the underlying physical mechanism is revealed.

2 Full-mode nonlinear flutter analysis method

2.1 Novel finite element model for nonlinear flutter analysis

In this section, a full-mode approach for nonlinear flutter analysis is established based on the full-mode linear flutter analysis method [13]. In the smooth flow, the governing equation of motion for a bridge can be written as:

$$\mathbf{M}_s\ddot{\mathbf{X}} + \mathbf{C}_s\dot{\mathbf{X}} + \mathbf{K}_s\mathbf{X} = \mathbf{F}_{\mathrm{se,non}}, \tag{1}$$

in which $\mathbf{M}_s$,$\mathbf{C}_s$ and $\mathbf{K}_s$ are the global mass, damping and stiffness matrices, respectively; $\mathbf{F}_{\mathrm{se,non}}$ is the vector of nodal nonlinear self-excited forces; $\mathbf{X}$,$\dot{\mathbf{X}}$ and $\ddot{\mathbf{X}}$ represent the nodal displacement, velocity and acceleration vectors, respectively.

The nonlinear self-excited forces (i.e., pitching moment, drag force, and lift force) distributed on a unit length of bridge deck could be described in terms of amplitude-dependent FDs as (e.g., [49])

$$\begin{cases} L_{\mathrm{se,non}}(t)=\frac{1}{2}\rho U^2(2b)\times \\ \quad \left(kH_1^*\frac{\dot{h}}{U}+kH_2^*\frac{b\dot{\alpha}}{U}+k^2H_3^*\alpha+k^2H_4^*\frac{h}{b}+kH_5^*\frac{\dot{p}}{U}+k^2H_6^*\frac{p}{b}\right) \\ D_{\mathrm{se,non}}(t)=\frac{1}{2}\rho U^2(2b)\times \\ \quad \left(kP_1^*\frac{\dot{p}}{U}+kP_2^*\frac{b\dot{\alpha}}{U}+k^2P_3^*\alpha+k^2P_4^*\frac{p}{b}+kP_5^*\frac{\dot{h}}{U}+k^2P_6^*\frac{h}{b}\right) \\ M_{\mathrm{se,non}}(t)=\frac{1}{2}\rho U^2(2b^2)\times \\ \quad \left(kA_1^*\frac{h}{U}+kA_2^*\frac{b\dot{\alpha}}{U}+k^2A_3^*\alpha+k^2A_4^*\frac{h}{b}+kA_5^*\frac{\dot{p}}{U}+k^2A_6^*\frac{p}{b}\right) \end{cases}, \tag{2}$$

in which ρ denotes the air density; U is the mean wind speed; $B = 2b$ is the width of bridge deck; $k = b\omega/U$ denotes the reduced circular frequency; h, α and p are the vertical, torsional and lateral displacements of the bridge deck, respectively; $\dot{h}$,$\dot{\alpha}$ and $\dot{p}$ denote the vertical, torsional and lateral velocity of the bridge deck, respectively; and H_i^*, P_i^* and A_i^* (i = 1,2⋯,6) are nonlinear flutter derivatives expressed in terms of vibration amplitude and reduced frequency k.

Converting the distributed self-excited forces of element e into equivalent nodal forces at ends, then the equivalent nodal forces of element e can be expressed as:

$$\mathbf{F}^e_{\text{se,non}} = \mathbf{K}^e_{\text{se,non}}\mathbf{X}^e + \mathbf{C}^e_{\text{se,non}}\dot{\mathbf{X}}^e, \tag{3}$$

in which $\mathbf{K}^e_{\text{se,non}}$ and $\boldsymbol{C}^e_{\text{se,non}}$ represent the aerodynamic stiffness and damping matrices of element e, respectively. $\dot{\mathbf{X}}^e$ and $\mathbf{X}^e$ donate the nodal velocity and displacement, respectively. If a lumped formulation is employed to derive the aerodynamic stiffness and damping matrices, the aeroelastic damping and stiffness matrices for element e can be written as:

$$\begin{aligned}\mathbf{K}^e_{\text{se,non}} &= \begin{bmatrix}\mathbf{K}^e_{\text{se,non1}} & 0\\ 0 & \mathbf{K}^e_{\text{se,non1}}\end{bmatrix},\\ \mathbf{C}^e_{\text{se,non}} &= \begin{bmatrix}\mathbf{C}^e_{\text{se,non1}} & 0\\ 0 & \mathbf{C}^e_{\text{se,non1}}\end{bmatrix},\end{aligned} \tag{4}$$

$$\mathbf{K}^e_{\text{se,non1}} = a\begin{bmatrix}0 & 0 & 0 & 0 & 0 & 0\\ 0 & H_4^*(k,A_r) & H_6^*(k,A_r) & bH_3^*(k,A_r) & 0 & 0\\ 0 & P_6^*(k,A_r) & P_4^*(k,A_r) & bP_3^*(k,A_r) & 0 & 0\\ 0 & bA_4^*(k,A_r) & bA_6^*(k,A_r) & b^2A_3^*(k,A_r) & 0 & 0\\ 0 & 0 & 0 & 0 & 0 & 0\\ 0 & 0 & 0 & 0 & 0 & 0\end{bmatrix}, \tag{5}$$

$$\mathbf{C}^e_{\text{se,non1}} = c\begin{bmatrix}0 & 0 & 0 & 0 & 0 & 0\\ 0 & H_1^*(k,A_r) & H_5^*(k,A_r) & bH_2^*(k,A_r) & 0 & 0\\ 0 & P_5^*(k,A_r) & P_1^*(k,A_r) & bP_2^*(k,A_r) & 0 & 0\\ 0 & bA_1^*(k,A_r) & bA_5^*(k,A_r) & b^2A_2^*(k,A_r) & 0 & 0\\ 0 & 0 & 0 & 0 & 0 & 0\\ 0 & 0 & 0 & 0 & 0 & 0\end{bmatrix}, \tag{6}$$

in which $c = L_{\text{e}}\rho Ubk/2$ and $a = L_{\text{e}}\rho U^2k^2/2$; $A_r(r = \alpha, p, h)$ is the amplitude; and L_{e} donates the length of element e.

The aerodynamic damping or stiffness matrices described by Eq. (4) can be simulated with the element Matrix27 in ANSYS. Therefore, a hybrid finite element model integrating one structural element with four Matrix27 elements $e1$, $e2$, $e3$ and $e4$ is formulated, in which $e1$ and $e2$ represent the nonlinear aeroelastic stiffness elements, while $e3$ and $e4$ represent the nonlinear aeroelastic damping elements, as shown in Fig. 1.

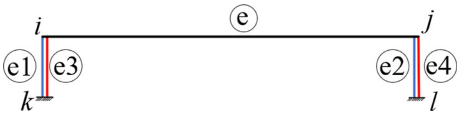

Fig. 1 Hybrid finite element model

Assembling all elemental matrices into global aerodynamic damping and stiffness matrices, one obtains

$$\mathbf{F}_{\text{se,non}} = \mathbf{K}_{\text{se,non}}\mathbf{X} + \mathbf{C}_{\text{se,non}}\dot{\mathbf{X}}, \tag{7}$$

in which $\boldsymbol{K}_{\text{se,non}}$ and $\boldsymbol{C}_{\text{se,non}}$ represent the global aerodynamic stiffness and damping matrices.

Substituting Eq. (7) into Eq. (1), the governing equation of the nonlinear wind-bridge coupled system can be written as:

$$\mathbf{M}_s\ddot{\mathbf{X}} + (\mathbf{C}_s - \mathbf{C}_{\text{se,non}})\dot{\mathbf{X}} + (\mathbf{K}_s - \mathbf{K}_{\text{se,non}})\mathbf{X} = \mathbf{0}. \tag{8}$$

Equation (8) is parameterized by vibration frequency, vibration amplitude and wind speed. For a finite element model with n DOFs, by the complex eigenvalue analysis of Eq. (8), a total of n conjugate pairs of complex eigenvectors and eigenvalues can be obtained. The conjugate pairs of complex eigenvalues λ_j and eigenvectors $\boldsymbol{\Phi}_j$ corresponding to the jth modal branch can be expressed as:

$$\lambda_j = (-\xi_j \pm i)\omega_j, \quad \boldsymbol{\Phi}_j = \mathbf{p}_j \pm i\mathbf{q}_j, \quad (j = 1, \ldots, n), \tag{9}$$

in which ξ_j and ω_j are the modal damping and frequency corresponding to the jth modal branch. Therefore, the three-dimensional motion of the bridge in physical coordinates corresponding to the jth modal branch can be written as:

$$\begin{aligned}\mathbf{X}_j = (\mathbf{p}_j + i\mathbf{q}_j)\mathrm{e}^{-\xi_j\omega_j t}\mathrm{e}^{i\omega_j t} + (\mathbf{p}_j\\ - i\mathbf{q}_j)\mathrm{e}^{-\xi_j\omega_j t}\mathrm{e}^{-i\omega_j t} = \mathbf{A}_j\mathrm{e}^{-\xi_j\omega_j t}\cos\left(\omega_j t - \boldsymbol{\phi}_j\right),\end{aligned} \tag{10}$$

where

$$\mathbf{A}_j = 2\left|\mathbf{p}_j + i\mathbf{q}_j\right|, \tag{11}$$

$$\boldsymbol{\phi}_j = \arctan(\mathbf{q}_j/\mathbf{p}_j), \tag{12}$$

in which $\boldsymbol{\phi}_j$ and $\mathbf{A}_j$ represent the vibration phase and amplitude, respectively, for all nodes of the bridge.

In this study, the damping of the bridge is assumed as the Rayleigh damping matrix:

$$\mathbf{C}_s = \alpha\mathbf{M}_s + \beta\mathbf{K}_s, \tag{13}$$

in which α and β can be determined by [50]

$$\alpha = 2\frac{\omega_{si}\omega_{sj}}{\omega_{sj}^2 - \omega_{si}^2}\left(\omega_{sj}\xi_{si} - \omega_{si}\xi_{sj}\right), \tag{14}$$

$$\beta = 2\frac{\omega_{si}\omega_{sj}}{\omega_{sj}^2 - \omega_{si}^2}\left(-\frac{\xi_{si}}{\omega_{sj}} + \frac{\xi_{sj}}{\omega_{si}}\right), \tag{15}$$

in which ξ_{sj} and ξ_{si} donate the damping ratio of the jth and ith structural mode, respectively; ω_{sj} and ω_{si} donate the circular frequency of the jth and ith structural mode, respectively.

2.2 Algorithm implementation in ANSYS

At a given wind speed, the participation information of each structural mode in coupled flutter cannot be known in advance, so the FDs along the span of bridge are unknown, and then, Eq. (8) cannot be determined. Actually, the participation information of each structural mode will also vary with the vibration amplitude.

2.2.1 Determination of flutter derivatives at different spanwise locations

In the present study, only the nonlinear self-excited force of the bridge deck is considered; therefore, Eq. (8) only depends on the motion amplitude of the deck at different spanwise locations. Obviously, the nodal vibration amplitude $r_0(x)$ of the deck at the spanwise location x for the jth modal branch can be obtained from $\mathbf{A}_j$ shown in Eq. (11), in which $r_0 = h_0, p_0, \alpha_0$ and essentially represent the amplitude shape of the bridge deck in the vertical, lateral and torsional directions, respectively.

In this study, the FDs are described as functions of vibration amplitude and reduced wind speed, so every point of the nonlinear wind-bridge coupled system in the space of vibration amplitude and reduced wind speed can be considered as a linear system. Therefore, the nonlinear full-mode flutter analysis becomes to calculate the linear modal properties of every point in this space. In addition, there is a need to determine a location x for amplitude searching during searching the modal properties in the space of vibration amplitude and wind speed due to the fact that the vibration amplitude of the bridge is different at different locations. In general, considering that the modal properties of the jth modal branch evolve from the jth structural mode, the location of amplitude searching for the jth modal branch usually should be determined as $x_{\max,j}$, the location of the maximum value of the jth structural mode shape. For instance, $x_{\max,j}$ should be determined as the mid-span of the bridge for the first symmetric torsional mode, while it should be determined as the 3/4 or 1/4 span of the bridge for the first antisymmetric torsional mode. For the jth modal branch, if the vibration amplitude of the location $x_{\max,j}$ is A_r, the vibration amplitude at location x can be determined by:

$$A_{r,x} = \frac{r_0(x)}{r_0(x_{\max,j})}A_r. \tag{16}$$

Then, the FDs at spanwise locations x for a given reduced wind speed U^* are obtained as:

$$A_i^*(x) = A_i^*\left(U^*, A_{r,x}\right), \quad H_i^*(x) = H_i^*\left(U^*, A_{r,x}\right), \quad (i = 1 \sim 6). \tag{17}$$

2.2.2 Solution of full-mode coupled nonlinear flutter

For a given amplitude A_r at the location $x_{\max,j}$ and a given wind speed U, the FDs at different spanwise locations are initially unknown because the participation information of each structural mode in bridge flutter is unknown in advance. Therefore, a preliminary iterative procedure for amplitude shape r_0 is needed to determine the vibration amplitude of each node along the span. An initial iterative amplitude shape generally can be set as $|r_j(x)|$, in which $r_j(x)$ is the jth structural mode shape. Then, the vibration amplitude at different locations x can be determined by:

$$A_{r,x} = \frac{|r_j(x)|}{|r_j(x_{\max,j})|}A_r. \tag{18}$$

After the FDs are determined, another iterative procedure for the modal frequency of the jth modal branch, which is same as the linear flutter analysis [12, 13], needs to be implemented to obtain the modal properties.

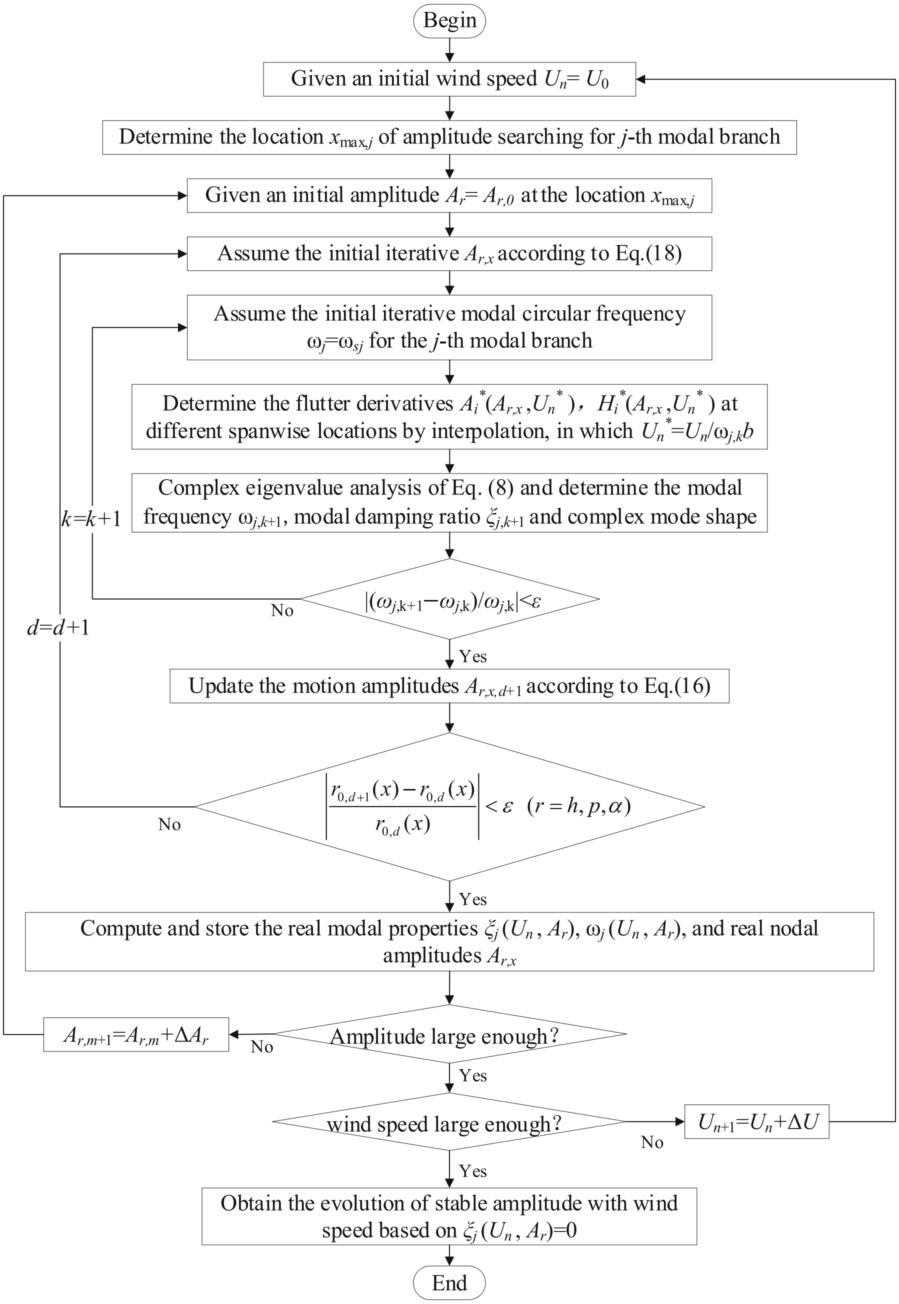

Fig. 2 The flowchart of the proposed full-mode nonlinear analysis framework

The above full-mode nonlinear analysis method can only consider the aerodynamic nonlinearity, and it involves a double-layer iterative procedure. To clarify the proposed full-mode nonlinear analysis framework more clearly, Fig. 2 demonstrates the specific flowchart by taking the calculation of the jth modal branch as an example. Besides, some main steps in the flowchart are introduced as follows:

(1) Set the initial calculated wind speed $U_n = U_0$;
(2) Set the location of amplitude searching $x_{\max,j}$;

(3) Set the initial vibration amplitude $A_r = A_{r,0}$ at the location $x_{\max,j}$ and set the initial iterative $A_{r,x}$ according to Eq. (18);

(4) Set the initial iterative modal frequency $\omega_j = \omega_{sj}$, where ω_{sj} is the frequency of the jth structural mode;

(5) Calculate the FDs $A_i^*(A_{r,x},\ U_n^*)$ and $H_i^*(A_{r,x},\ U_n^*)$ at different locations by interpolation, where $U_n^* = U_n/(\omega_{j,k}b)$;

(6) Conduct the complex eigenvalue analysis of Eq. (8) and obtain the modal damping ratio, modal frequency and complex mode shape of the jth modal branch at the present iteration;

(7) Compare modal frequency $\omega_{j,k+1}$ with $\omega_{j,k}$ obtained by the last iteration. If $\left|(\omega_{j,k+1} - \omega_{j,k})/\omega_{j,k}\right| < \varepsilon$, terminate the iteration and go to step 8, otherwise, return to step 4;

(8) Based on the amplitude shape r_0 obtained in the present iteration, update the vibration amplitudes $A_{r,x}$ at different locations according to Eq. (16);

(9) Define a convergence factor for the amplitude shape iteration as

$$\mu(x) = \left|\frac{r_{0,d+1}(x) - r_{0,d}(x)}{r_{0,d}(x)}\right|, \quad (r = h, p, \alpha), \tag{19}$$

where d donates the dth (d = 1, 2, 3, 4, 5···) iteration step. When the convergence factors μ for all nodes of the main girder are smaller than the tolerance ε, terminate the iteration and go to step 10, otherwise, return to step 4;

(10) Compute and store the real modal properties ξ_j (A_r, U_n), ω_j (A_r, U_n) and the nodal amplitudes $A_{r,x}$ along the bridge's span at wind speed U_n and vibration amplitude A_r;

(11) Gradually increase the amplitude A_r by ΔA_r, and repeat steps 3 $\sim$ 10 until a maximum vibration amplitude $A_{r,\max}$ given for searching is reached;

(12) Gradually increase the wind speed U_n by ΔU, and repeat steps 1 $\sim$ 11 until a maximum wind speed $U_{n,\max}$ given for searching is reached;

(13) Based on the real modal properties ω_j (A_r, U_n), ξ_j (A_r, U_n) and $A_{r,x}(A_r, U_n)$ in the space of vibration amplitude and wind speed, the evolution of stable amplitudes with wind speed (i.e., the 3D post-flutter response of the bridge) can be obtained by searching the points where the modal damping ξ_j (A_r, U_n) = 0.

3 Time-dependent nonlinear numerical scheme

3.1 Time-dependent linear self-excited force model

The self-excited forces per unit span length induced by arbitrary structural motion can be expressed in terms of convolution integrals using impulse response functions as [51]

$$L_{\mathrm{se}}(t) = \frac{1}{2}\rho U^2 \int_{-\infty}^{t} \big(I_{Lh}(t-\tau)h(\tau) + I_{Lp}(t-\tau)p(\tau) + I_{L\alpha}(t-\tau)\alpha(\tau)\big)\mathrm{d}\tau, \tag{20}$$

$$D_{\mathrm{se}}(t) = \frac{1}{2}\rho U^2 \int_{-\infty}^{t} \big(I_{Dh}(t-\tau)h(\tau) + I_{Dp}(t-\tau)p(\tau) + I_{D\alpha}(t-\tau)\alpha(\tau)\big)\mathrm{d}\tau, \tag{21}$$

$$M_{\mathrm{se}}(t) = \frac{1}{2}\rho U^2 \int_{-\infty}^{t} \big(I_{Mh}(t-\tau)h(\tau) + I_{Mp}(t-\tau)p(\tau) + I_{M\alpha}(t-\tau)\alpha(\tau)\big)\mathrm{d}\tau, \tag{22}$$

where I_{fx} (f = L, D, M; x = h, p, α) denotes the impulse function of the self-excited forces, in which the subscripts represent the corresponding force component. Taking the impulse function of the lift force induced by the vertical motion (i.e., I_{Lh}) as an example, according to the rational function (RF) approximation [52–54], I_{Lh} can be further written as:

$$I_{Lh}(t) = A_1\delta(t) + A_2\frac{b}{U}\dot{\delta}(t) + A_3\frac{b^2}{U^2}\ddot{\delta}(t) + \delta(t)\sum_{n=4}^{m}A_n - \sum_{n=4}^{m}A_n d_n\frac{U}{b}\exp\left(-\frac{d_nU}{b}t\right), \tag{23}$$

where δ is the unit impulse function; A_1, A_2, A_3, A_n, d_n (n = 4, 5…, m) are frequency-independent coefficients, which can be determined by the nonlinear least-square method based on the obtained FDs [54]; m was taken as 5 in this study. The third term in Eq. (23) represents the aerodynamic force caused by the acceleration term, which is usually small and neglected. Then, substituting Eq. (23) into Eq. (20), the aerodynamic lift force induced by the vertical motion can be obtained as follows:

$$L_{seh}(t) = \frac{1}{2}\rho U^2\left[A_1h(t) + A_2\frac{b}{U}\dot{h}(t)\right] + \frac{1}{2}\rho U^2\sum_{n=4}^{m}A_n\int_{-\infty}^{t}e^{-\frac{d_nU}{b}(t-\tau)}\dot{h}(\tau)d\tau. \tag{24}$$

Similarly, the expressions for the other self-excited force components $L_{\mathrm{se}\alpha}$, $M_{\mathrm{se}h}$ and $M_{\mathrm{se}\alpha}$ can be obtained. Since the time-dependent linear self-excited force model is finally described as a form of rational functions, it is simply called as linear RFs model here.

3.2 Time-dependent nonlinear self-excited force model

The aforementioned linear RFs model is unable to describe the nonlinear characteristics of self-excited forces varying with amplitude. To this end, similar to using amplitude-dependent FDs to describe nonlinear self-excited forces in Eq. (2), a time-dependent nonlinear self-excited force model using amplitude-dependent impulse response functions can be expressed as:

$$L_{\mathrm{se,non}}(t,\hat{r}) = \frac{1}{2}\rho U^2\int_{-\infty}^{t}(I_{Lh}(t-\tau,\hat{r})h(\tau). + I_{Lp}(t-\tau,\hat{r})p(\tau) + I_{L\alpha}(t-\tau,\hat{r})\alpha(\tau))\mathrm{d}\tau, \tag{25}$$

$$D_{\mathrm{se,non}}(t,\hat{r}) = \frac{1}{2}\rho U^2\int_{-\infty}^{t}(I_{Dh}(t-\tau,\hat{r})h(\tau). + I_{Dp}(t-\tau,\hat{r})p(\tau) + I_{D\alpha}(t-\tau,\hat{r})\alpha(\tau))\mathrm{d}\tau, \tag{26}$$

$$M_{\mathrm{se,non}}(t,\hat{r}) = \frac{1}{2}\rho U^2\int_{-\infty}^{t}(I_{Mh}(t-\tau,\hat{r})h(\tau). + I_{Mp}(t-\tau,\hat{r})p(\tau) + I_{M\alpha}(t-\tau,\hat{r})\alpha(\tau))\mathrm{d}\tau, \tag{27}$$

where $\hat{r}$(r = h, p, α) denote the vibration amplitude. It should be noted that the self-excited drag force and the self-excited forces caused by the lateral displacement p are ignored in the following analysis. Thus, Eqs. (25)–(27) can be further simplified as:

$$L_{\mathrm{se,non}}(t,\hat{r}) = \frac{1}{2}\rho U^2\int_{-\infty}^{t}(I_{Lh}(t-\tau,\hat{r})h(\tau) + I_{L\alpha}(t-\tau,\hat{r})\alpha(\tau))\mathrm{d}\tau = L_{\mathrm{se}h,\mathrm{non}}(t,\hat{r}) + L_{\mathrm{se}\alpha,\mathrm{non}}(t,\hat{r}), \tag{28}$$

$$M_{\mathrm{se,non}}(t,\hat{r}) = \frac{1}{2}\rho U^2\int_{-\infty}^{t}(I_{Mh}(t-\tau,\hat{r})h(\tau) + I_{M\alpha}(t-\tau,\hat{r})\alpha(\tau))d\tau = M_{\mathrm{se}h,\mathrm{non}}(t,\hat{r}) + M_{\mathrm{se}\alpha,\mathrm{non}}(t,\hat{r}). \tag{29}$$

It is presumed that when the FDs corresponding to a group of discrete motion amplitudes $\hat{r}_k$ (k = 1, 2,…, n) are obtained, the RF models corresponding to a group of discrete motion amplitudes $\hat{r}_k$ can also be determined using the method mentioned in Sect. 3.1. Then, the time-dependent nonlinear self-excited force model under arbitrary amplitudes $\hat{r}$ can be approximately determined by interpolation as:

$$L_{\mathrm{se,non}}(t,\hat{r}) = \gamma_{r,k}\cdot L_{\mathrm{se}\alpha}(t,\hat{r}_k) + \gamma_{r,k+1}\cdot L_{\mathrm{se}\alpha}(t,\hat{r}_{k+1}) + \gamma_{r,k}\cdot L_{\mathrm{se}h}(t,\hat{r}_k) + \gamma_{r,k+1}\cdot L_{\mathrm{se}h}(t,\hat{r}_{k+1}), \tag{30}$$

$$M_{\mathrm{se,non}}(t,\hat{r}) = \gamma_{r,k}\cdot M_{\mathrm{se}\alpha}(t,\hat{r}_k) + \gamma_{r,k+1}\cdot M_{se\alpha}(t,\hat{r}_{k+1}) + \gamma_{r,k}\cdot M_{\mathrm{se}h}(t,\hat{r}_k) + \gamma_{r,k+1}\cdot M_{\mathrm{se}h}(t,\hat{r}_{k+1}), \tag{31}$$

in which:

$$\hat{r}_k < \hat{r} < \hat{r}_{k+1}, \tag{32}$$

$$\gamma_{r,k} = \frac{\hat{r}_{k+1} - \hat{r}}{\hat{r}_{k+1} - \hat{r}_k}, \quad \gamma_{r,k+1} = \frac{\hat{r} - \hat{r}_k}{\hat{r}_{k+1} - \hat{r}_k}, \tag{33}$$

where $k = 1,2,3\cdots n$; n is the number of discrete amplitudes. The larger the n within a certain amplitude range, the more accurate the nonlinear characteristics of self-excited forces can be described by Eqs. (30) and (31). Besides, to ensure that the nonlinear self-excited force model described by Eqs. (30) and (31) can be applied to the arbitrary motion with the nonzero mean value, the limiting behavior of Eqs. (30) and (31) need to meet the quasi-steady characteristics of wind load after the change of structure attitude. Thus, one obtains:

$$L_{\mathrm{se}h}(t \to \infty) = 0, \quad M_{\mathrm{se}h}(t \to \infty) = 0, \tag{34}$$

$$\begin{aligned} L_{\mathrm{se}\alpha}(t \to \infty) &= 0.5\rho U^2 b C_L' \Delta\alpha \\ &= F_L(\alpha_0 + \Delta\alpha) - F_L(\alpha_0), \end{aligned} \tag{35}$$

$$\begin{aligned} M_{\mathrm{se}\alpha}(t \to \infty) &= 0.5\rho U^2 b^2 C_M' \Delta\alpha \\ &= F_M(\alpha_0 + \Delta\alpha) - F_M(\alpha_0), \end{aligned} \tag{36}$$

where F_M, F_L are quasi-steady wind load; α_0 is initial angle of attack, $\Delta\alpha$ is the increment of attack angle or the increment of the mean torsional displacement. According to the above conditions, it can be obtained that the constraints for identifying rational function coefficients in the nonlinear self-excited force model are:

$$A_{Mh1} = A_{Lh1} = 0, \, A_{L\alpha 1} = bC_L'(\alpha_0), \, A_{M\alpha 1} = b^2 C_M'(\alpha_0). \tag{37}$$

After integrating the nonlinear self-excited force model described by Eqs. (30) and (31) and the nonlinear finite element model by using APDL offered by ANSYS, a time-dependent nonlinear numerical scheme can be implemented in ANSYS software. By using this scheme, the whole evolution process of 3D post-flutter response considering structural nonlinearity and aerodynamic nonlinearity under arbitrary wind speed can be obtained. In addition, it should be noted that the nonlinear flutter analysis method described in this section is a time-domain method while the full-mode nonlinear flutter analysis method described in Sect. 3 is a frequency-domain method, in which the frequency-domain method can only consider the aerodynamic nonlinearity.

4 Parameters identification and validation

4.1 Engineering background

As shown in Fig. 3, a single-span steel-truss girder suspension bridge with a main span of 1650 m and two side spans of 518 m and 502 m in the preliminary design scheme is taken as a case study herein. The bridge includes four main cables, which is the first time adopted in the design scheme. The sag/span ratio of the outer main cable is 1/10.79, while that of the inner main cable is 1/11.61. As shown in Fig. 3b and c, the double-deck steel-truss girder is 9.5 m high and 32 m wide.

Firstly, to obtain the dynamic characteristics of the bridge as accurately as possible, a refined spatial-truss-girder finite element model was established by ANSYS, as shown in Fig. 4. The two towers and the main steel truss are simulated with spatial beam elements, while the hangers and the main cables are modeled by spatial link elements. In addition, the whole steel bridge panel is simulated with shell elements. However, the refined model is a very complex model and it has 23,136 elements and 11,970 nodes in total, which makes its transient analysis very time-consuming and also requires huge storage demand. To this end, a simplified equivalent-single-girder finite element model (or called single-spine girder model), who only has 2153 elements and 1368 nodes in total, was established according to the stiffness and mass distribution equivalence of the main girder in all directions. More details about the modeling method of the equivalent-single-girder model can be found in our previous study [54]. The dynamic characteristics of the two finite element models are compared in Table 1, and it can be found that they are in good agreement. Therefore, the single-spine girder model will be adopted to the full-mode analysis and transient analysis of nonlinear flutter in Sect. 5. Additionally, it should be noted that, for example, “V–A-1” in Table 1 represents the first antisymmetric vertical mode shape.

4.2 Amplitude-dependent flutter derivatives

The amplitude-dependent FDs of the bridge deck are obtained from free-vibration wind tunnel tests of the section model [34, 49]. The section model tests are conducted at the wind tunnel of the Research Center of

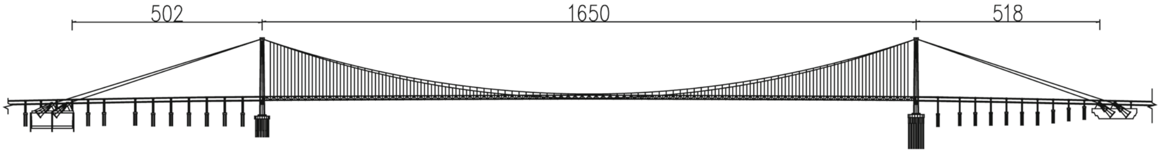

(a) Arrangement of the bridge (unit: m)

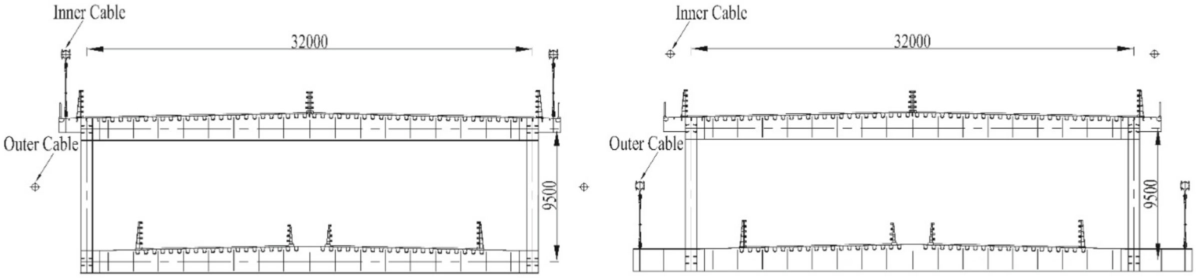

(b) Section at inner slings (unit: mm)

(c) Section at outer slings (unit: mm)

Fig. 3 The structural dimension of the bridge in the preliminary design scheme

Fig. 4 The refined finite element model of the bridge

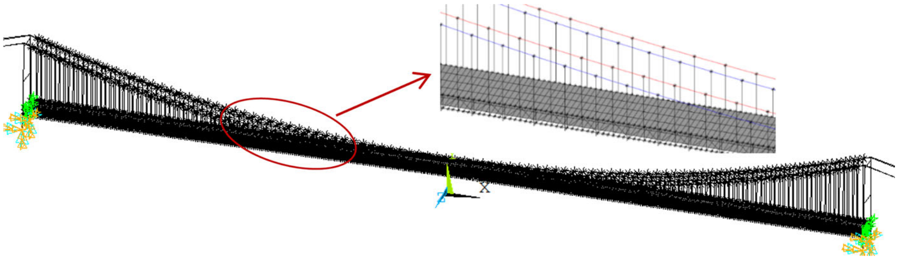

Table 1 Dynamic characteristics of the bridge

Mode number	Mode shape[a]	Frequency f (Hz)		Error (%)
		The refined model	The single-spine girder model	
1	L–S-1	0.0470	0.0471	0.21
2	V–A-1	0.0886	0.0884	-0.23
3	L–A-1	0.1018	0.1027	0.88
4	V–S-1	0.1162	0.1159	-0.26
5	V–A-1 (coupled LF)	0.1358	0.1348	-0.74
6	V–S-2	0.1621	0.1613	-0.49
7	T–S-1 (coupled minor L–S-2)	0.1799	0.1795	-0.22
8	L–S-2 (coupled minor T–S-1)	0.1897	0.1903	0.32
9	T–A-1	0.2111	0.2107	-0.19
10	V–A-2	0.2119	0.2124	0.24

[a] L, lateral; V, vertical; T, torsional; LF, longitudinal floating; S, symmetrical; A, asymmetrical

Wind Engineering and Wind Environment in Changsha University of Science and Technology, as shown in Fig. 5. The main dynamic parameters of section model tests are given in Table 2, in which case B is obtained by increasing the structural damping on the basis of case A, while case C is obtained by changing

Fig. 5 Section model in wind tunnel

Table 2 Main dynamic parameters of all cases (initial attack angle 0°)

Cases	m (kg/m)	I (kg m^2/m)	f_{h0} (Hz)	$f_{\alpha 0}$ (Hz)	$f_{\alpha 0}/f_{h0}$
A	17.7508	1.0702	1.7055	2.57	1.51
B	17.7508	1.0702	1.72	2.601	1.51
C	16.5223	1.4486	1.7677	2.209	1.25

the mass m and mass moment of inertia I on the basis of case A. It should be noted that the structural damping of cases A $\sim$ C is amplitude-dependent due to nonlinear factors [29], as shown in Fig. 6. Based on the amplitude-dependent FDs obtained from case A, as shown in Fig. 7, the stable amplitudes of nonlinear flutter for cases A $\sim$ C can be calculated by the closed-form solution method [49] and they are compared with the experimental results, as shown in Fig. 8. It can be found that the calculated values agree well with the experimental values for all cases, which indicates that the amplitude-dependent FDs shown in Fig. 7 are accurate and reliable and thus can be used to the following analysis. As shown in Fig. 7, A_1^* and A_4^* are somewhat scattered. It is mainly because the contribution of A_1^* and A_4^* to the modal properties of flutter is relatively small, as also stated in other studies [2, 33, 35], which thus lead the identification of A_1^* and A_4^* is easy to be interfered by noises in the recorded displacement signal. Besides, the noise in signal may also vary with wind speed and amplitude, which will inevitably further enhance the scatter of A_1^* and A_4^*. In addition, it can be found that the FDs H_2^*, H_3^*, A_1^*, A_2^*, A_3^* and A_4^* all exhibit a certain nonlinear dependence on the torsional amplitude, while the FDs H_1^* and H_4^* have no dependence on amplitude. Consequently, when adopting the above two methods for nonlinear flutter analysis of this bridge, only the torsional amplitude needs to be concerned. However, for bridge decks whose FDs are dependent on the lateral or vertical amplitude, the corresponding amplitude should be concerned. Besides, it should be noted that since the nonlinearity of aerodynamic force is described by the amplitude-dependent FDs, only the nonlinearity from the first-order aerodynamic force component has been considered herein. The contribution of higher-order aerodynamic force components is negligible, which has been directly validated by the

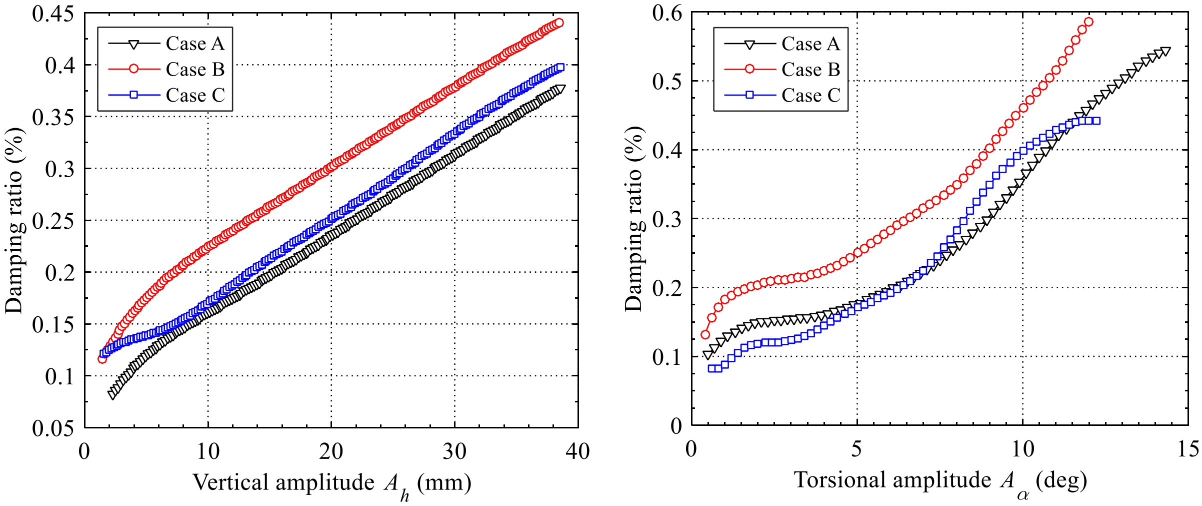

(a) Vertical structural damping

(b) Torsional structural damping

Fig. 6 Nonlinear characteristics of structural damping for all cases A $\sim$ C

Fig. 7 Amplitude-dependent FDs of the bridge deck [34, 49]

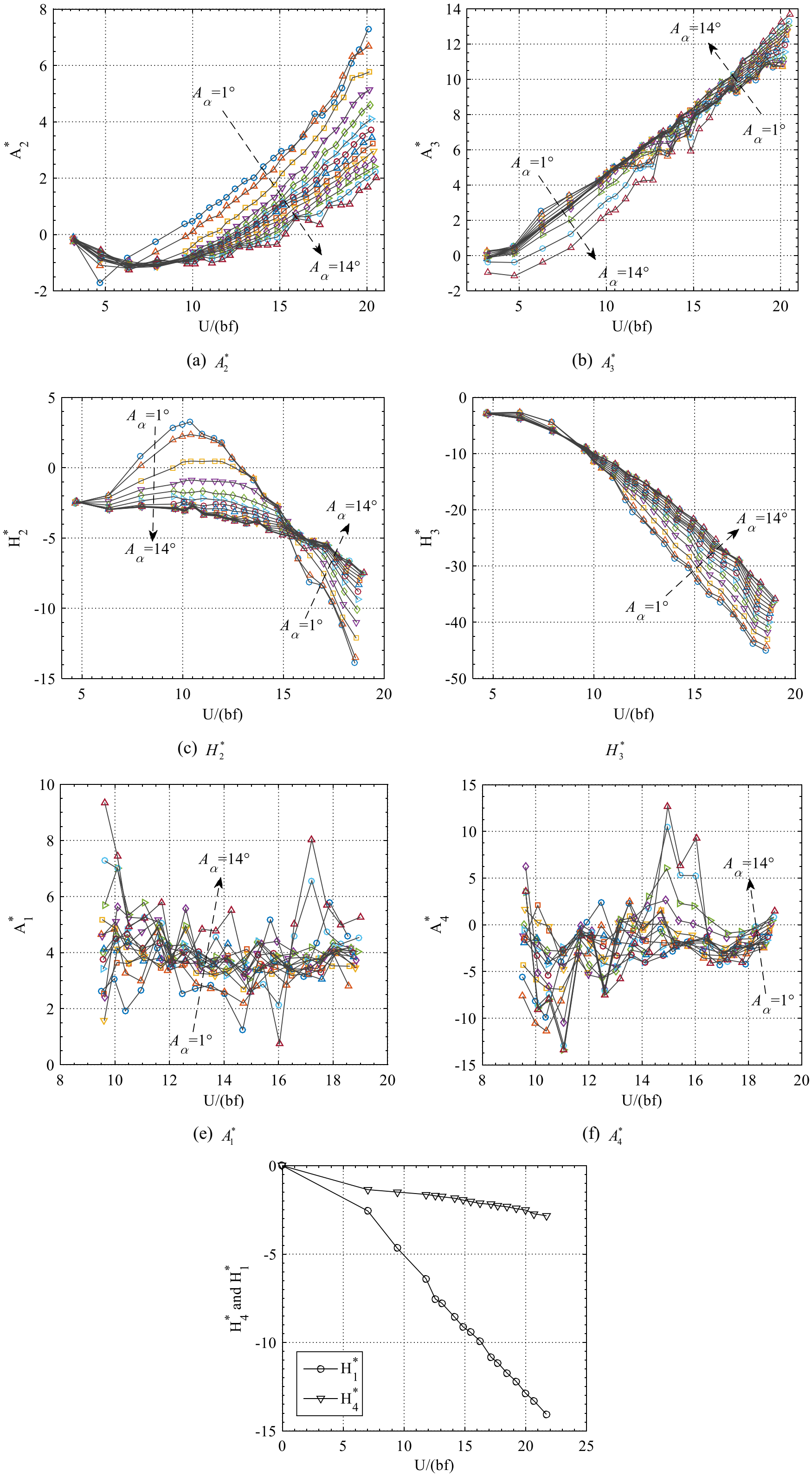

(a) A_2^*

(b) A_3^*

(c) H_2^*

H_3^*

(e) A_1^*

(f) A_4^*

(g) H_1^* and H_4^*

results shown in Fig. 8. In fact, whether it is airfoil or complex bridge deck section, many studies have been shown that the higher-order aerodynamic force components have negligible effects on nonlinear flutter or vortex-induced vibration [28, 35, 37, 49, 55–57].

4.3 Identification and validation of coefficients in amplitude-dependent RFs model

The identified coefficients of the RFs model under amplitudes ranging from 1° to 14° for the steel-truss bridge deck are shown in Tables 3, 4, 5, and 6. For long-span suspension bridges, it should be noted that the bridge deck will exhibit vibration behavior with a nonzero mean value due to the significant geometric nonlinear effect. Thus, the constraints shown in Eq. (37) should be and have been taken into account in the identification of coefficients to ensure that the amplitude-dependent RFs model can be used for arbitrary motion with nonzero mean value. Figure 9 further displays the experimental values and the fitted values (back-calculated by the RFs model) of the amplitude-dependent FDs, in which only the amplitudes 1° $\sim$ 2° $\sim$ 13° are given for a better comparison among results. It can be seen that the fitted values agree well with the experimental values. It should be noted that the deviation of H_2^* between the experimental and fitted values is relatively large at the low reduced wind speed, but it has little effect on the prediction of post-flutter response occurring at relatively high reduced wind speeds. In addition, the scatter of A_1^* and A_4^* is relatively large, but the fitted values capture the overall variation trend of the experimental values.

To further validate the accuracy of the above-identified coefficients in amplitude-dependent RFs model, the closed-form solution method of bimodal coupled nonlinear flutter [49] was adopted to calculate the post-flutter response. The fundamental symmetric vertical bending mode (i.e., mode 4) and the fundamental symmetric torsional mode (i.e., mode 7), as shown in Fig. 10, were selected in the bimodal

Table 3 Coefficients of L_{seh} under different amplitudes

Amplitude (°)	A_1	A_2	A_4	A_5	d_4	d_5
–	0	− 17.9942	− 4460.1334	4522.223	2.1	2.12

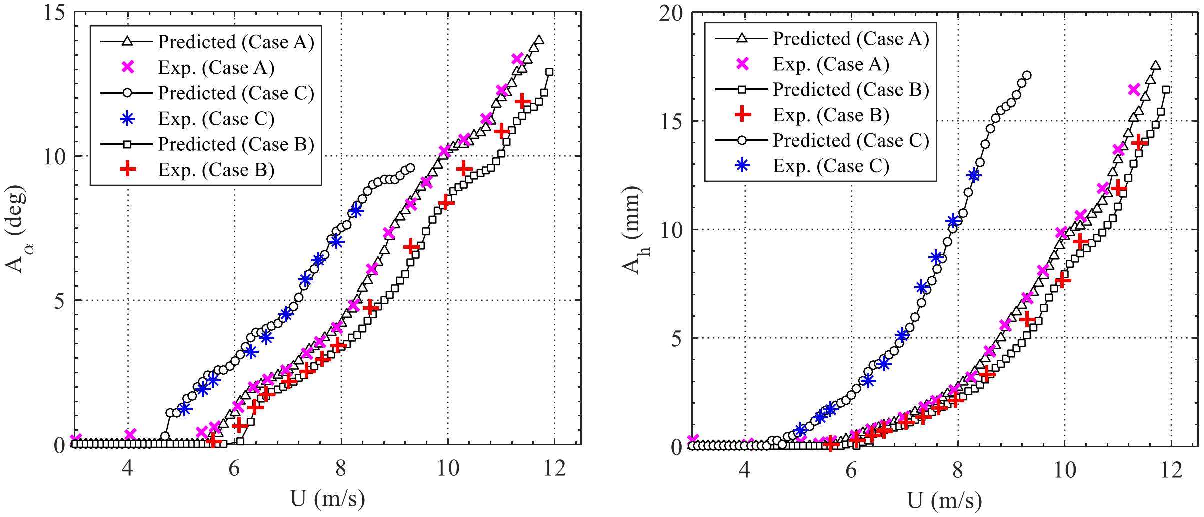

(a) Torsional stable amplitude

(b) Vertical stable amplitude

Fig. 8 Comparison of experimental and predicted values for all cases A $\sim$ C

Table 4 Coefficients of $L_{\text{se}\alpha}$ under different amplitudes

Amplitude (°)	A_1	A_2	A_4	A_5	d_4	d_5
1	118.7168	− 76.9239	− 364.5151	432.3657	0.136	1.4
2	118.7168	− 154.924	711.212	− 346.2209	2.0804	0.1232
3	118.7168	9.0618	− 351.6245	143.0982	0.116	0.62
4	118.7168	5.617	− 397.3277	155.3634	0.1116	0.32
5	118.7168	− 10.5943	− 473.9836	228.8646	0.106	0.22
6	118.7168	− 23.1521	− 728.1258	483.7662	0.1076	0.16
7	118.7168	− 33.4884	567.845	− 809.8092	0.1424	0.1004
8	118.7168	− 40.7086	− 1434.7867	1194.5721	0.1004	0.1204
9	118.7168	− 48.6651	− 1478.2212	1242.5769	0.1004	0.1204
10	118.7168	− 52.5492	− 1493.5972	1261.4263	0.1004	0.1204
11	118.7168	− 53.416	1258.1454	− 1488.1854	0.1204	0.1004
12	118.7168	− 53.5389	− 1473.3566	1245.0186	0.1004	0.1204
13	118.7168	− 52.606	1224.062	− 1451.4881	0.1204	0.1004
14	118.7168	− 51.9954	1207.1518	− 1434.31	0.1204	0.1004

Table 5 Coefficients of $M_{\text{se}\alpha}$ under different amplitudes

Amplitude (°)	A_1	A_2	A_4	A_5	d_4	d_5
1	73.3386	− 596.9666	376.0756	780.9517	0.8004	0.2772
2	73.3386	− 568.0822	1345.1051	− 430.3009	0.2332	0.1004
3	73.3386	− 733.3883	− 357.2629	1301.5371	0.1004	0.2484
4	73.3386	− 441.3449	− 1427.1263	1216.5314	2.12	0.3668
5	73.3386	− 660.4305	− 821.3399	1120.2697	2.12	0.3416
6	73.3386	− 925.8215	147.5772	914.6707	0.1004	0.3748
7	73.3386	− 919.1351	840.2294	228.3741	0.4024	0.1004
8	73.3386	− 904.9328	286.57	776.5374	0.1004	0.4204
9	73.3386	− 893.9194	324.2686	723.4956	0.1004	0.4256
10	73.3386	− 883.6051	367.3299	670.1928	0.1004	0.4404
11	73.3386	− 814.5074	402.9647	567.69	0.1004	0.4204
12	73.3386	− 634.6006	403.4069	405.7245	0.3004	0.1004
13	73.3386	534.6521	− 2668.2071	822.3676	2.12	0.1612
14	73.3386	1633.7856	875.9644	− 5224.0231	0.1524	2.1

coupled nonlinear flutter analysis. Figure 11 compares the stable amplitude responses calculated based on the experimental and fitted FDs, respectively. It can be seen that the responses under three different structural damping ratios (0%, 0.3% and 0.5%) are all in good agreement. It should be noted that the agreement between the two results is relatively poor at some wind speeds, which is mainly caused by the relatively large difference between the experimental and fitted FDs at some reduced wind speeds. It also gives a piece of important information that the post-flutter response is very sensitive to the amplitude-dependent flutter derivatives, and thus, the accurate identification of the amplitude-dependent flutter derivatives is the premise of accurately evaluating the post-flutter response.

Table 6 Coefficients of $M_{\mathrm{se}h}$ under different amplitudes

Amplitude (°)	A_1	A_2	A_4	A_5	d_4	d_5
1	0	374.0272	676,028.8442	− 676,587.1025	0.9324	0.9328
2	0	358.7005	120,573.5838	− 120,947.3636	0.6192	0.6204
3	0	277.4826	28.8825	− 284.2366	0.1004	0.98
4	0	160.4117	− 2779.5262	2704.1972	0.3204	0.3124
5	0	140.6502	2446.6648	− 2503.9017	0.274	0.2804
6	0	143.0279	42,515.505	− 42,577.1678	0.2948	0.2952
7	0	141.2115	− 21,336.6057	21,276.063	0.2912	0.2904
8	0	116.4468	− 69.733	29.0968	0.3568	0.1004
9	0	− 106.3774	1,079,571.823	− 1,079,080.344	1.3252	1.3248
10	0	80.6058	230.3214	− 243.0658	0.1004	0.1204
11	0	161.2068	− 110.8085	35.0984	0.56	0.1004
12	0	285.4071	− 262.6829	55.6201	0.78	0.1004
13	0	245.2003	76,056.7753	− 76,212.0002	0.4048	0.4056
14	0	287.4627	177,688.7311	− 177,874.5846	0.4084	0.4088

5 Influence of geometric nonlinearity on post-flutter responses

The geometric nonlinear effects of long-span suspension bridges mainly originate from the following aspects: (1) stress-stiffening effect, which mainly includes the gravity stiffness of the main cable and the geometric stiffness of the suspender caused by the dead load of the bridge deck. (2) Sag effect of the main cable caused by the dead load of the bridge deck, which will result in a certain reduction of the stiffness of the main cable. (3) Large deformation effect due to the action of wind load, where the structural equilibrium equation should be re-established at the position after each minor deformation. The influence of the stress stiffening effect can be taken into account by setting "STIFF, ON" when the transient analysis was conducted in the ANSYS software. Besides, when "NLGEOM, ON" is used, both the stress stiffening effect and the large deformation effect are included, though this case is labeled as large deformation effect hereafter in the transient analysis.

5.1 3D nonlinear flutter analysis for a suspension bridge with four main cables

It can be seen from Table 1 that the frequency ratio of T–S-1 to V–S-1 is 1.548, which is much less than the frequency ratio of T–A-1 to V–A-1, 2.384. Besides, the frequency of T–A-1 is higher than that of T–S-1. Therefore, the nonlinear flutter of this bridge is dominated by the first symmetric torsional modal branch (or called the 7-th modal branch). To investigate the influence of geometric nonlinearity on post-flutter responses, six different cases of 3D nonlinear flutter analysis are conducted, as shown in Table 7. It should be noted that the full-mode nonlinear flutter analysis (i.e., cases 1 $\sim$ 2) is based on the fitted FDs. Therefore, the influence of geometric nonlinearity on nonlinear flutter can be investigated and quantified by comparing the results of frequency-domain analysis (i.e., cases 1 $\sim$ 2) and time-domain analysis (i.e., cases 3 $\sim$ 6). In addition, the classic Rayleigh damping model is adopted in cases 1 $\sim$ 6 and the Rayleigh damping coefficient α and β is determined based on mode 4 (V–S-1) and mode 7 (T–S-1). It should be noted that both the stress stiffening effect and large deformation effect are considered in cases 4 and 6 though labeled as large deformation effect hereafter.

The damping mechanism of real bridge structure is very complicated. On the one hand, it is too difficult to obtain the structural damping characteristics of real bridge structure under large amplitudes, especially the structural damping ratio of torsional modes under large torsional amplitudes. On the other hand, there is no mathematical model that can describe the evolution mechanism of nonlinear damping for real bridge structures under large amplitudes currently. Therefore, it is almost impossible to accurately simulate the post-flutter response of a real long-span bridge at present. However, in general, with the increase in amplitude,

Fig. 9 Experimental versus fitted values of FDs under different amplitudes

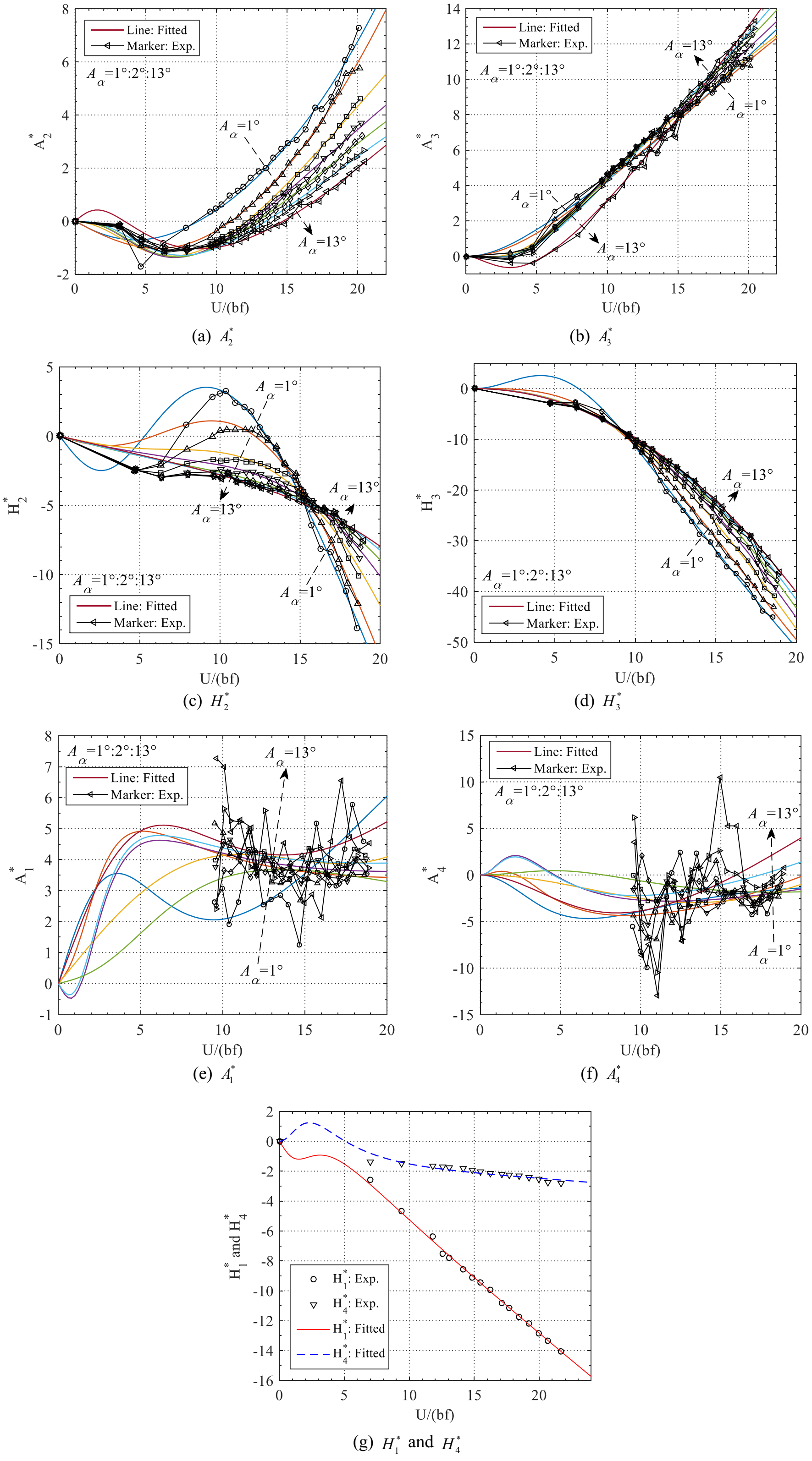

(a) A_2^* (b) A_3^*

(c) H_2^* (d) H_3^*

(e) A_1^* (f) A_4^*

(g) H_1^* and H_4^*

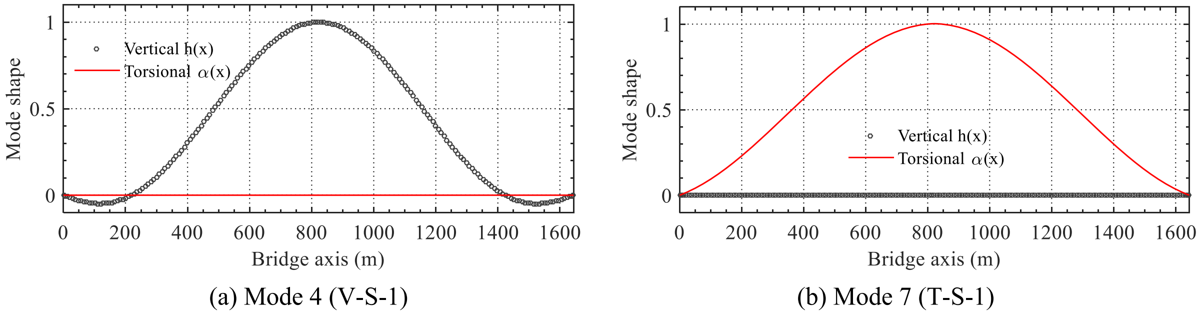

(a) Mode 4 (V-S-1) (b) Mode 7 (T-S-1)

Fig. 10 Bridge mode shapes

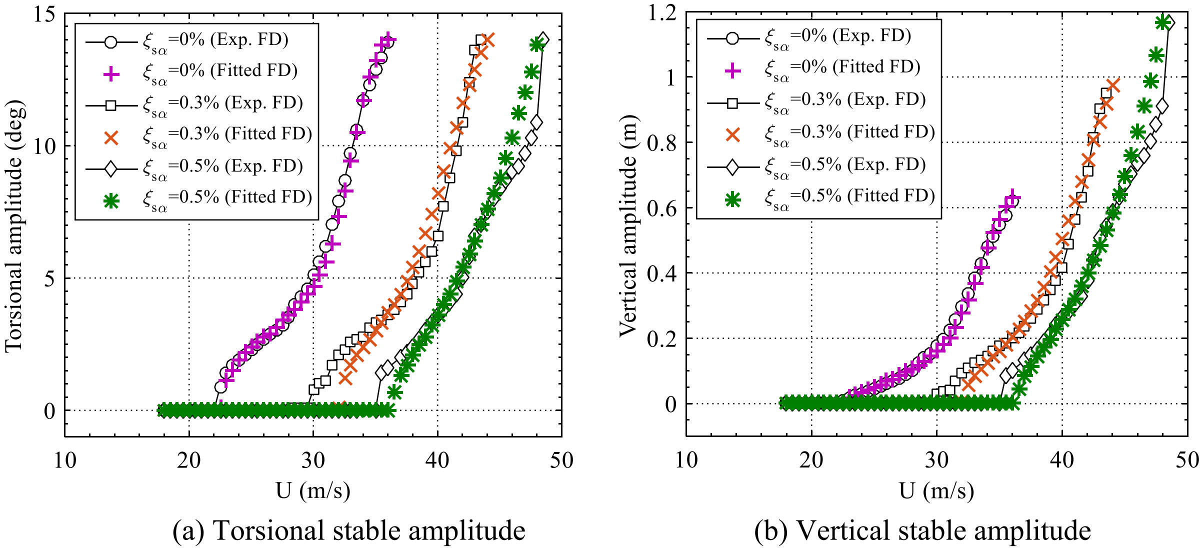

(a) Torsional stable amplitude (b) Vertical stable amplitude

Fig. 11 Stable amplitude responses calculated based on the experimental and fitted FDs

Table 7 Cases of 3D nonlinear flutter analysis

Case	Method	ξ_s (%)	Geometric nonlinear effect
Case 1	Frequency-domain analysis (full-mode)	0	–
Case 2	Frequency-domain analysis (full-mode)	0.3	–
Case 3	Time-domain analysis	0	Stress stiffening effect
Case 4	Time-domain analysis	0	Large deformation effect
Case 5	Time-domain analysis	0.3	Stress stiffening effect
Case 6	Time-domain analysis	0.3	Large deformation effect

the frictional energy dissipation at the joints of components of real structure will become more significant, and thus, the structural damping will increase with the increase in amplitude. Accordingly, it is conservative to evaluate the post-flutter responses of real structures by adopting the linear damping ratio given by the wind resistance design specifications. The present study is not intended to completely and accurately investigate the post-flutter behavior of real bridges, but rather to more truly evaluate the post-flutter response, quantify the impact of geometric nonlinearity on the post-flutter responses and reveal the corresponding mechanism. In addition, it should be noted that the Rayleigh damping will change with the displacement due to the structural stiffness $\boldsymbol{K}_s$ in Eq. (13) changing with the displacement under large motion amplitude. Therefore, individually quantifying the influence of geometric nonlinearity on nonlinear flutter can only be based on the cases without considering the structural damping (i.e., cases 1, 3, 4), which will be discussed later.

The nonlinear post-flutter response is greatly affected by the calculation time step Δt in the time-domain analysis, as shown in Fig. 12. It can be found that when Δt is 0.06 s or 0.02 s, the torsional stable amplitude is about 3.7° or 4.6°, respectively, with a difference of 0.9°. A relatively large time step Δt will underestimate the amplitude. However, when Δt is 0.01 s or 0.005 s, the torsional stable amplitude is about 4.91° or 4.96°, respectively, with a very slight difference. Considering the calculation cost, the time step Δt is taken as 0.01 s in the following time-domain analysis.

5.2 Influence of geometric nonlinearity on stable amplitude

Figure 13 displays the time history of displacement at the mid-span obtained by the time-domain analysis method and a typical bending-torsional coupled LCO can be observed. For the torsional displacement, the evolution of amplitude considering the stress stiffening effect agree well with that considering the large deformation effect, and the mean value of the response is basically zero. For the vertical displacement, the two are in good agreement at the small amplitude stage but gradually deviates as the amplitude increases. Besides, it can be seen that the mean value of the vertical displacement is close to zero at the small amplitude stage and increases gradually from zero as the amplitude increases, indicating that the bridge deck is gradually lifted up. Relatively speaking, the bridge deck considering large deformation effect is lifted up higher due to the more significant geometric nonlinearity compared with that only considering the stress stiffening effect. It should be noted that the behavior with a nonzero mean vibration cannot be predicted by the frequency-domain method because the geometric nonlinear effect cannot be considered (though aerodynamic nonlinear effect is included).

The evolution of the mid-span stable amplitudes with wind speed for cases 1 ∼ 6 in Table 7 is shown in Fig. 14. For the cases without structural damping (i.e., cases 1, 3, and 4), it can be observed that the stable amplitudes obtained by the frequency-domain method (i.e., case 1) agree well with that obtained by the time-domain method (i.e., case 3 and 4) when the amplitude is small ($< 4°$) due to the insignificant nonlinear effect. With the further increase of stable amplitude ($> 4°$), the results of case 3 and case 4 are gradually smaller than those of case 1, and this trend is more obvious in case 4 than in case 3. It indicates that the geometric nonlinear effect induced by the large deformation becomes more significant than that induced by the stress stiffening with the increase in amplitude. Besides, the results of case 4 become smaller and smaller than those of case 1 with the increase of stable amplitude, which indicates that the large deformation effect becomes more and more significant with the increase in vibration amplitude. Figure 15 further compares the stable amplitudes along the span of the bridge for cases 1, 3 and 4 when U = 32 m/s, and it can be seen that not only the amplitudes of the full span are reduced but also the

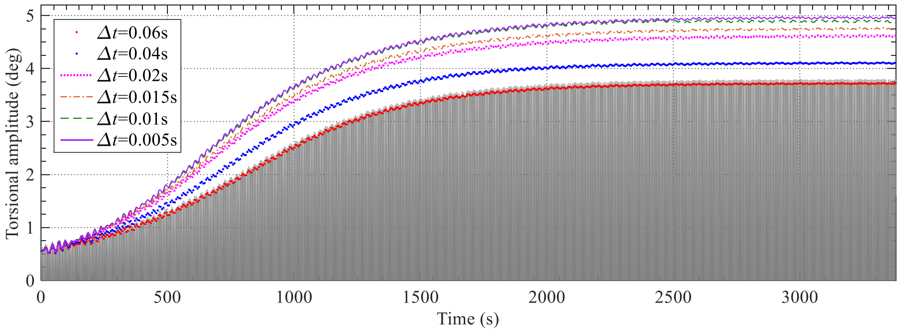

Fig. 12 Effect of time step Δt on post-flutter response (mid-span, U = 30 m/s, ξ_s = 0%)

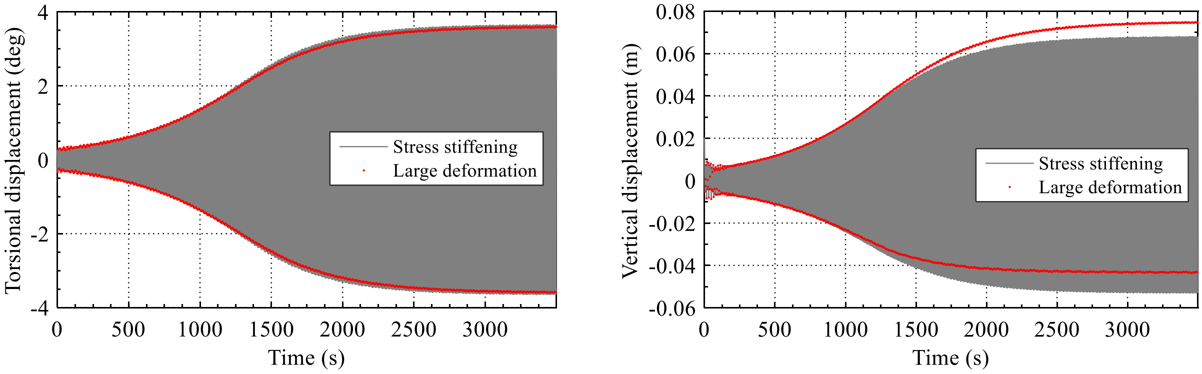

(a) Torsional displacement

(b) Vertical displacement

Fig. 13 Time histories of displacements at mid-span for cases 3 and 4 (U = 28 m/s; ξ_s = 0)

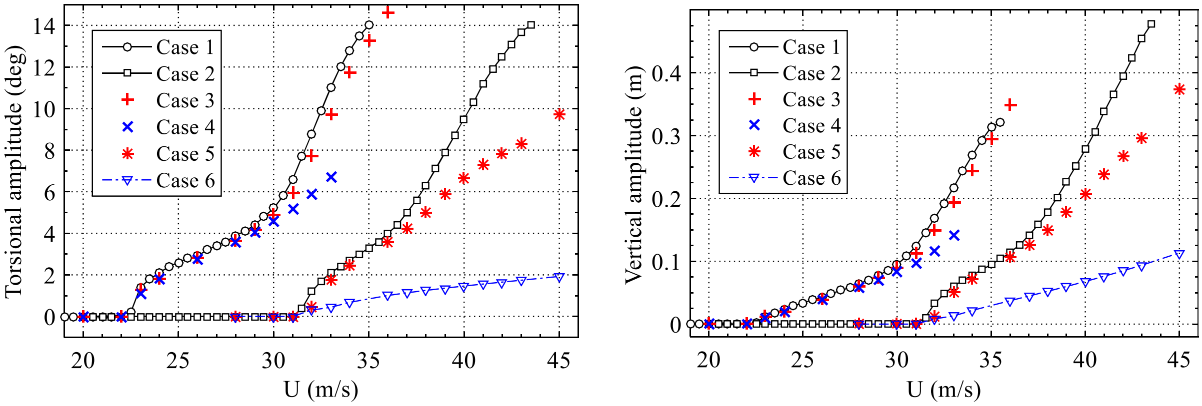

(a) Torsional stable amplitude

(b) Vertical stable amplitude

Fig. 14 Evolution of stable amplitude at mid-span with wind speed for cases 1 ~ 6

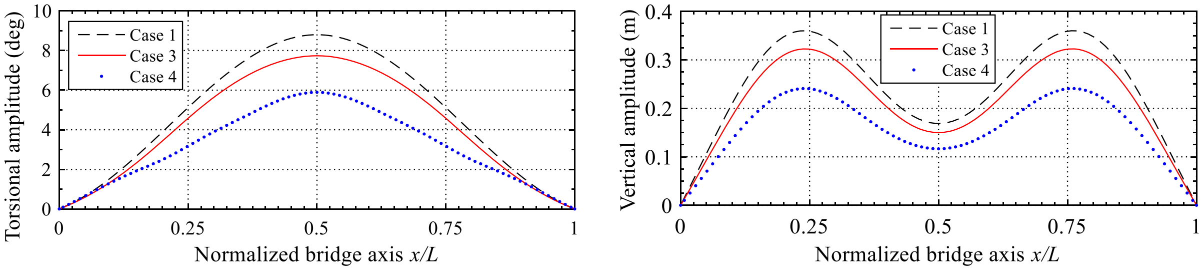

(a) Torsional stable amplitude

(b) Vertical stable amplitude

Fig. 15 Stable amplitudes along the span of the bridge for cases 1, 3, and 4 (U = 32 m/s; ξ_s = 0)

amplitude shape of the bridge deck is changed significantly due to the large deformation effect.

In summary, the large deformation effect can significantly reduce the stable amplitudes of post-flutter when the amplitude is large enough, and thus, the large deformation effect should be taken into account when the amplitude is relatively large. However, it should be noted that although the geometric nonlinearity has little influence on the stable amplitudes when the vibration amplitude is small (< 4°), it has a significant influence on the mean value of the vertical displacement, as shown in Fig. 13. Therefore, it cannot be concluded that the geometric nonlinearity can be ignored when the amplitude of this bridge is less than 4°, which will be further discussed later.

For the cases with structural damping ratio ξ_s = 0.3% (i.e., cases 2, 5, and 6), it can be observed from Fig. 14 that the stable amplitudes of case 2 agree well with that of case 5 when the amplitude is small (< 4°). However, as the amplitude further increases (> 4°), the stable amplitudes of case 5 become gradually smaller than those of case 2. After the large deformation effect is considered (i.e., case 6), the stable amplitudes are reduced to a greater extent. Besides, even if the amplitude is small (< 4°), the stable amplitude of case 6 is much smaller than that of case 2.

The above analysis shows that the influence of geometric nonlinearity on post-flutter responses is different between considering and not considering structural damping. To investigate the reason, Figs. 16 and 17 further display the free-decay responses of structural mode 4 (V–S-1) and mode 7 (T–S-1), respectively, under a large initial excitation. For mode 4, it can be found that the displacement responses between considering stress stiffening effect and large deformation effect are in good agreement. Moreover, the structural damping ratio of mode 4 remains at about 0.3% and hardly varies with the vertical amplitude. For mode 7, the damping ratio within 3° is maintained at 0.3% when only the stress stiffening effect is considered. With the further increase of amplitude, the damping ratio starts to increase and reaches about 0.45% when the vibration amplitude reaches 3.7°. After the large deformation effect is also taken into account, the damping ratio within 0.5° is maintained at 0.3% and then the damping ratio increases rapidly with the increase in amplitude. When the amplitude reaches 2.7°, the damping ratio even increased to 1.7%. The above analysis indicates that the stress stiffening effect and large deformation effect have little influence on the vertical stiffness of the bridge deck but have a great influence on the torsional stiffness of suspension bridges. As a result, the Rayleigh damping in the torsional direction increases significantly with the increase in amplitude, which is one of the main reasons for the sharp decrease in the stable amplitude after the large deformation effect is considered.

Although it is known that the structural damping of real bridges will increase with the increase in vibration amplitude due to various factors, whether the above-mentioned amplitude-dependent behavior of Rayleigh damping truly describes a physical damping mechanism of real bridges still needs to be validated by relevant research. Therefore, the physical mechanism for the influence of geometric nonlinearity on the post-flutter will be mainly discussed among the cases without structural damping.

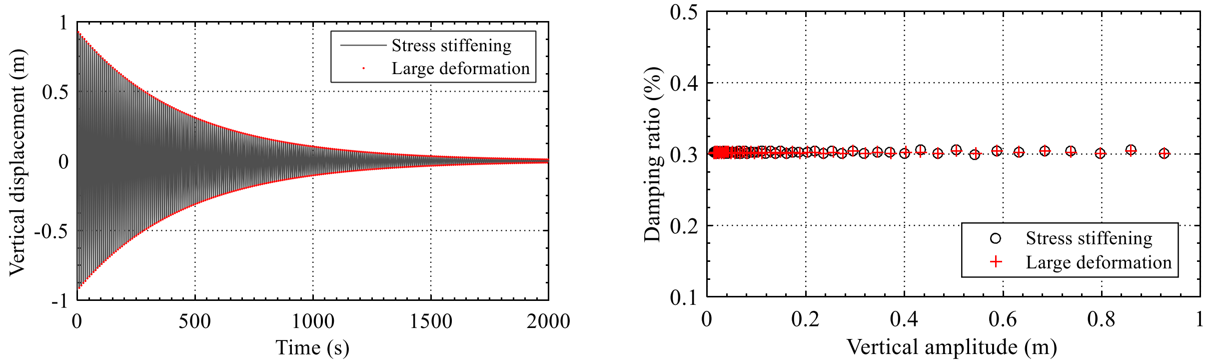

(a) Vertical displacement

(b) Damping ratio vs vertical amplitude

Fig. 16 Characteristics of free-decay responses at the mid-span of structural mode 4

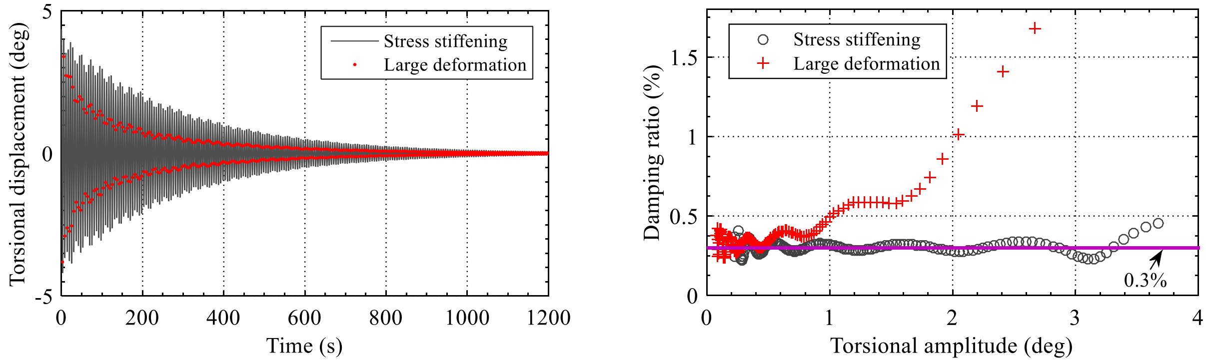

(a) Torsional displacement (b) Damping ratio vs torsional amplitude

Fig. 17 Characteristics of free-decay responses at the mid-span of structural mode 7

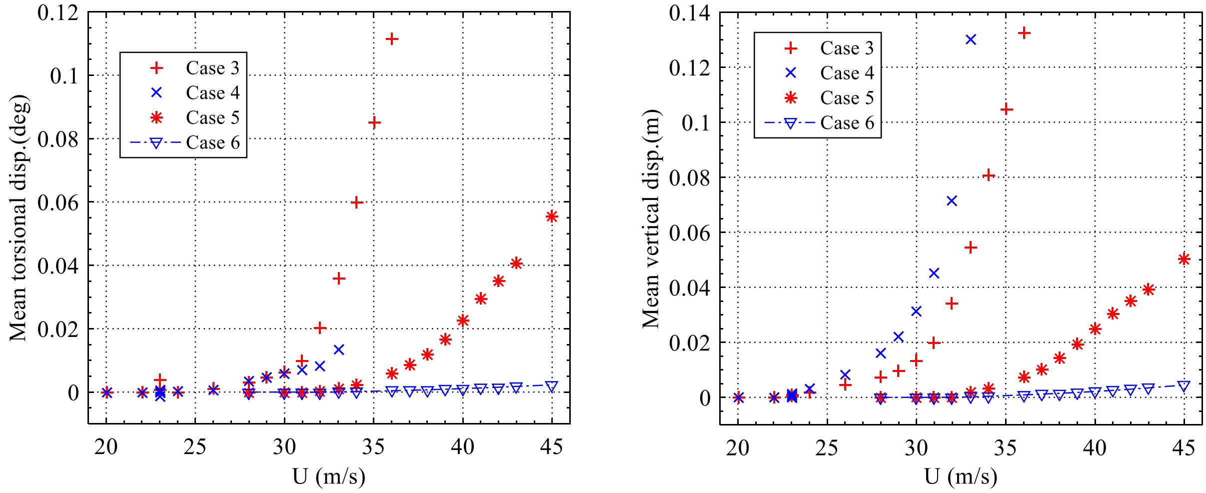

(a) Mean torsional displacement (b) Mean vertical displacement

Fig. 18 Evolution of mean displacement at mid-span with wind speed at the stable amplitude stage

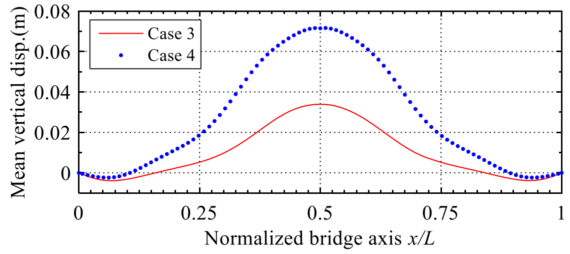

Fig. 19 Mean vertical displacement along the bridge's span at the stable amplitude stage (U = 32 m/s; ξ_s = 0)

5.3 Influence of geometric nonlinearity on mean displacements

Figure 18 displays the evolution of the mid-span mean displacement with wind speed at the sable amplitude stage. It can be found that both the mean values of the vertical displacement and torsional displacement exhibit nonzero behavior, and they both increase with the increase in stable amplitude. Since the mean torsional displacement is negligible, it will not be discussed in depth. Careful observation shows that even when the

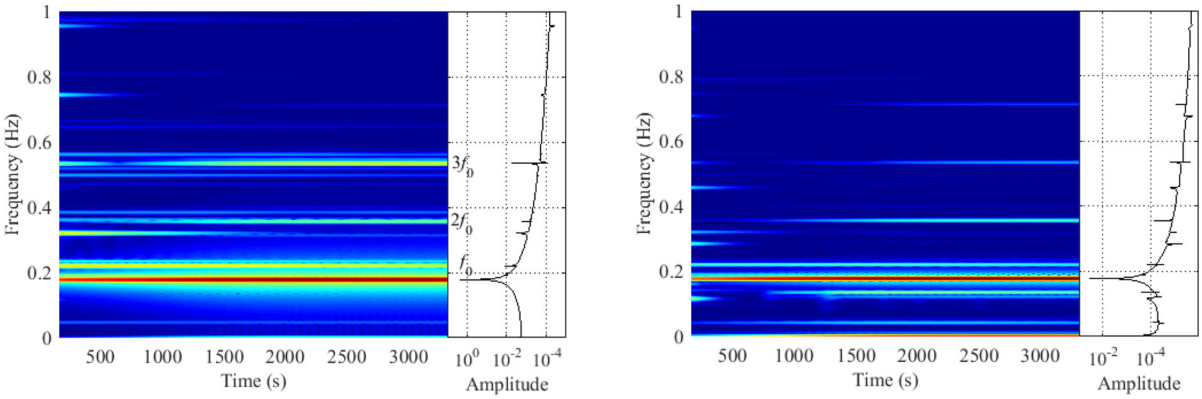

(a) Torsional displacement (b) Vertical displacement

Fig. 20 Time–frequency spectra of the corresponding responses considering stress stiffening effect in Fig. 13

stable amplitude is small (within 4°), there is a relatively significant mean vertical displacement. Therefore, although the geometric nonlinearity has a small influence on the stable amplitude within a small vibration amplitude (within 4° here) but will cause relatively significant mean vertical displacement. From this point of view, even if the vibration amplitude is relatively smaller, geometric nonlinearity also should be considered. The larger the amplitude, the more significant the geometric nonlinearity and thus the larger the mean vertical displacement. Figure 19 further shows the mean vertical displacement along the bridge's span at the stable amplitude stage when $U = 32$ m/s. It can be found that the mean vertical displacement of the bridge deck forms an uplift shape that approximates the first symmetrical vertical bending mode shape. In addition, the mean vertical displacement of case 4 is larger than that of case 3 because the geometric nonlinear effect of large deformation is much stronger than that of stress stiffening.

5.4 Super-harmonic resonance behavior induced by geometric nonlinearity

The main physical mechanism of the geometric nonlinear effect reducing the stable amplitudes will be further discussed in this section from the perspective of the whole evolution process of 3D responses.

5.4.1 Cases without structural damping

As mentioned earlier, the influence of geometric nonlinearity on post-flutter will be mainly discussed based on the cases without structural damping. Figures 20 and 21 show the time–frequency spectra of the corresponding responses shown in Fig. 13. When only the stress stiffening effect is considered (i.e., Fig. 20), it can be seen that a weak third harmonic frequency component $3f_0$ (f_0 is the fundamental harmonic frequency of flutter) gradually appears in the torsional displacement with the increase of amplitude (amplitude increases with time, shown in Fig. 13), while there are no higher harmonic frequency components in the vertical displacement. After the large deformation effect is taken into account (i.e., Fig. 21), not only the frequency component $3f_0$ in the torsional displacement becomes more significant, but also the significant higher harmonic frequency components $2f_0$, $3f_0$ and $4f_0$ appear in the vertical displacement at the same time. When the wind speed is further increased to 32 m/s, as shown in Fig. 22, one can observe that both the torsional and vertical amplitudes considering large deformation effect gradually become smaller than those only considering stress stiffening effect when the amplitudes increase to a certain extent. Similarly, Figs. 23 and 24 further give the time–frequency spectra of the corresponding responses in Fig. 22. It can be found that the higher harmonic frequency components in the responses have been enhanced compared with Figs. 20 and 21 due to the larger vibration amplitudes. This enhancement effect is mainly featured by increasing the amplitude of higher harmonic frequency components, as well as the emergence of new higher harmonic frequency components.

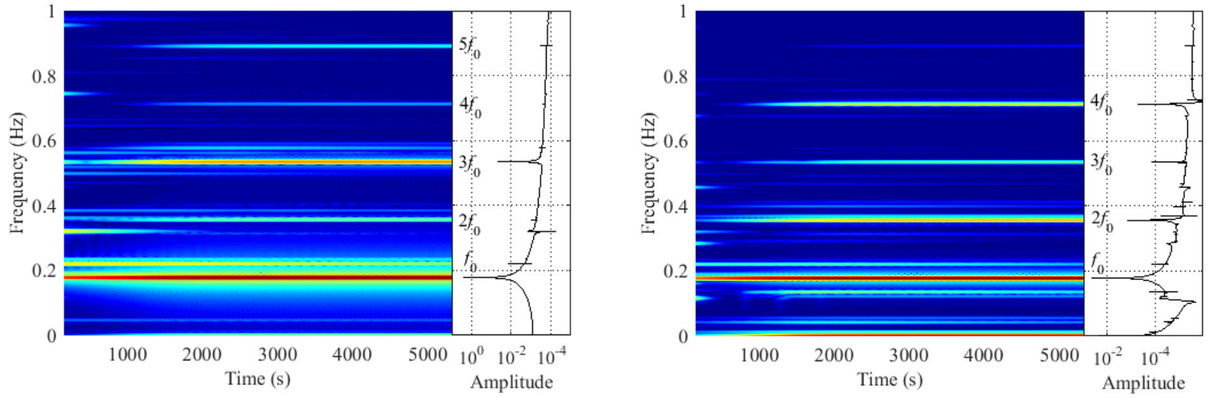

(a) Torsional displacement (b) Vertical displacement

Fig. 21 Time–frequency spectra of the corresponding responses considering large deformation effect in Fig. 13

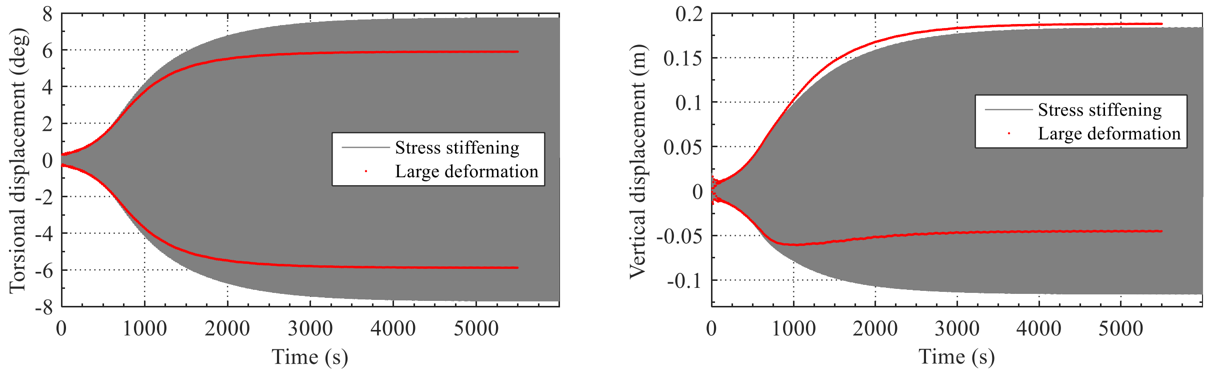

(a) Torsional displacement (b) Vertical displacement

Fig. 22 Time histories of displacements at mid-span of case 3 and case 4 ($U = 32$ m/s; $\xi_s = 0$)

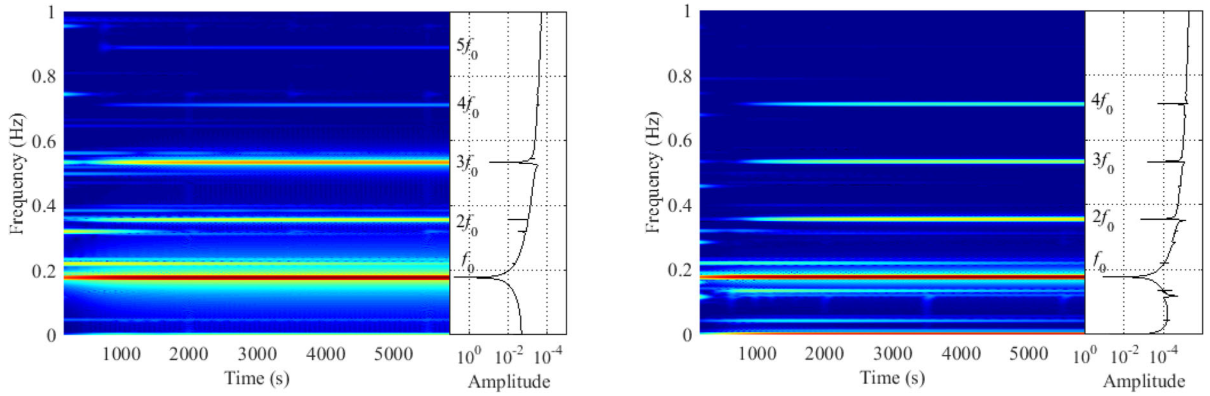

(a) Torsional displacement (b) Vertical displacement

Fig. 23 Time–frequency spectra of the corresponding responses considering stress stiffening effect in Fig. 22

The evolution of 3D vibration shape of the bridge deck in one vibration cycle at the stable amplitude stage is further shown in Figs. 25 and 26, in which the different lines represent the displacement of the bridge deck at different times. When only the stress stiffening effect is considered (i.e., Fig. 25), one can observe that the vibration in the torsional direction is mainly characterized by a T–S-1 mode shape but with significant higher-order torsional vibration shapes involved (such as the third symmetric torsional mode shape) at small torsional displacements. In addition, the vibration in the vertical direction is mainly characterized by a shape that couples V–S-1 and V–S-2, which indicates that the structural mode 6 (V–S-2) also contributes to the post-flutter. A more detailed discussion can be found in our previous study [49]. Similarly, the significant higher-order vertical vibration shapes (such as the third symmetric vertical mode shape) can also be observed at small vertical displacements. After the large deformation effect is taken into account (i.e., Fig. 26), it can be found that the vibration shape in the torsional direction has deviated far from the T–S-1 shape (mainly deviates from the sinusoidal waveform). Besides, the more significant higher-order torsional and vertical vibration shapes are observed in the torsional and vertical vibration

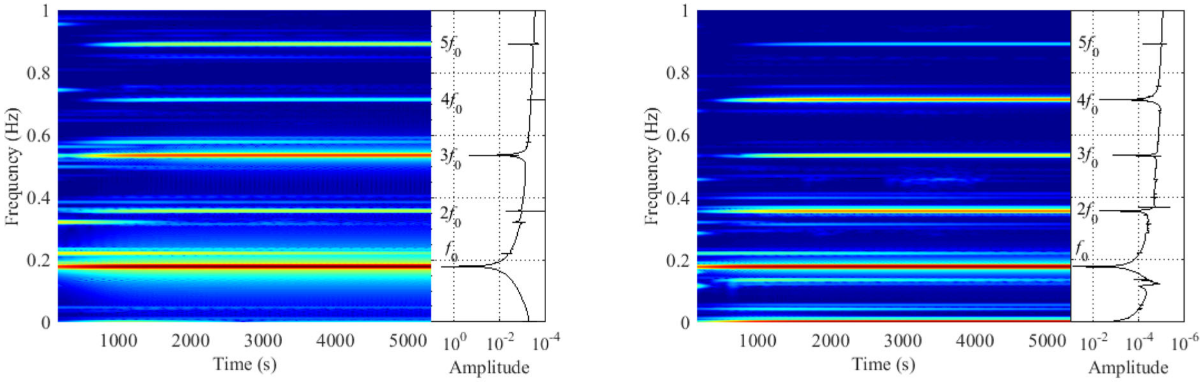

(a) Torsional displacement

(b) Vertical displacement

Fig. 24 Time–frequency spectra of the corresponding responses considering large deformation effect in Fig. 22

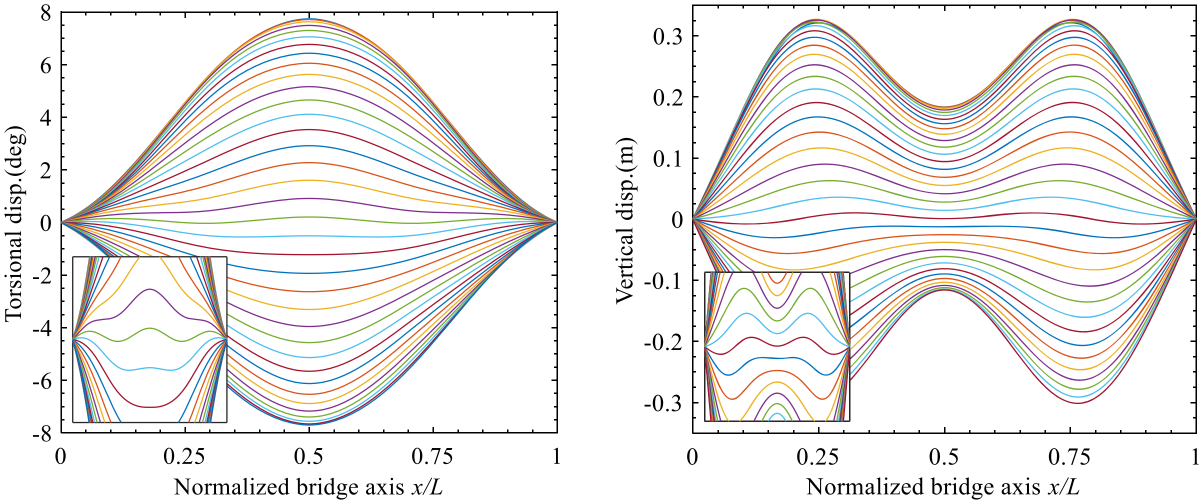

(a) Torsional displacement

(b) Vertical displacement

Fig. 25 3D vibration shape of the bridge deck in one vibration cycle at the stable amplitude stage (U = 32 m/s; ξ_s = 0; stress stiffening effect) displacements, respectively. Another noteworthy aspect is that the asymmetry of the vertical vibration is also becoming more significant compared with that only considering stress stiffening effect. This asymmetry is mainly characterized by the amplitude of the upward vibration being significantly larger than that of the downward vibration, as well as the "saddle shape" formed by the downward vibration being significantly deeper than that formed by the upward vibration.

In fact, there should be a correlation between the high-order vibration shapes in the displacement responses and the higher harmonic frequency components in the response spectra. Thus, the displacement responses considering large deformation effect can be

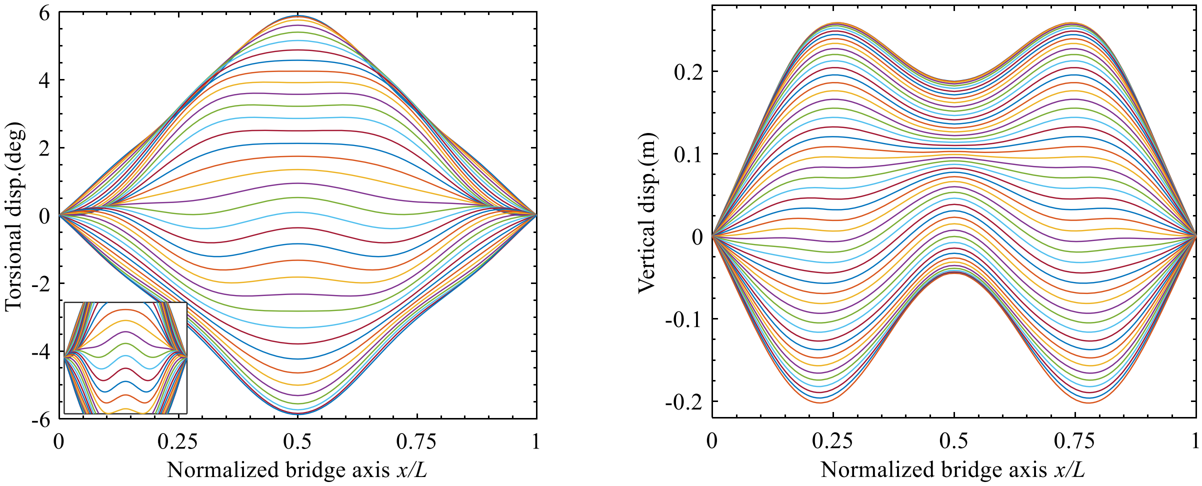

(a) Torsional displacement (b) Vertical displacement

Fig. 26 3D vibration shape of the bridge deck in one vibration cycle at the stable amplitude stage (U = 32 m/s; ξ_s = 0; large deformation effect)

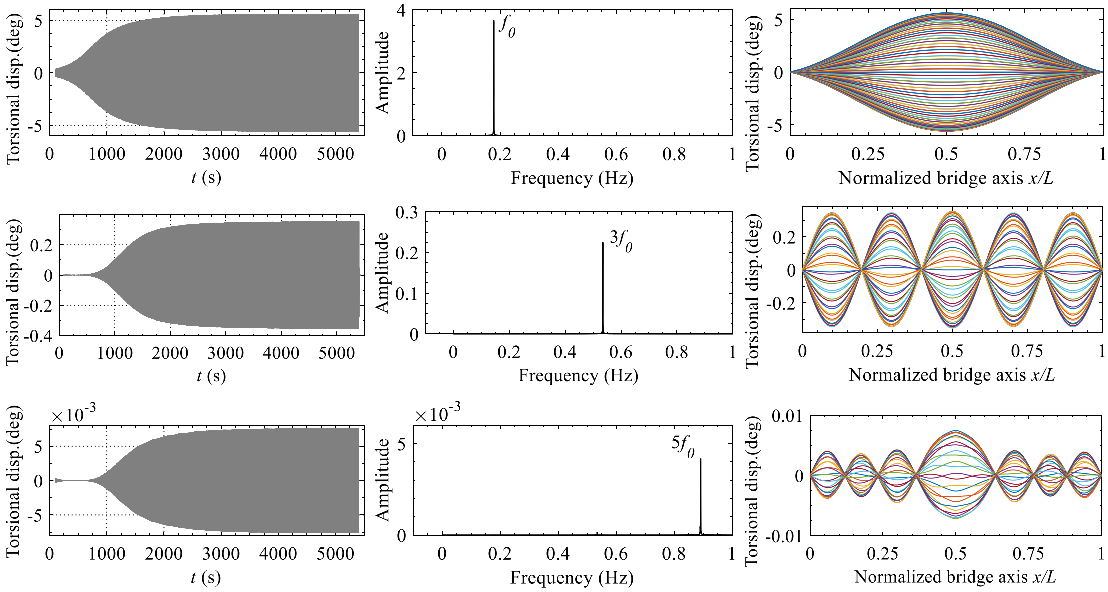

(a)Mid-span displacement component (b) Spectrum of displacement component (c)Vibration shape of displacement component

Fig. 27 Characteristics of torsional displacement components (U = 32 m/s; ξ_s = 0; large deformation effect)

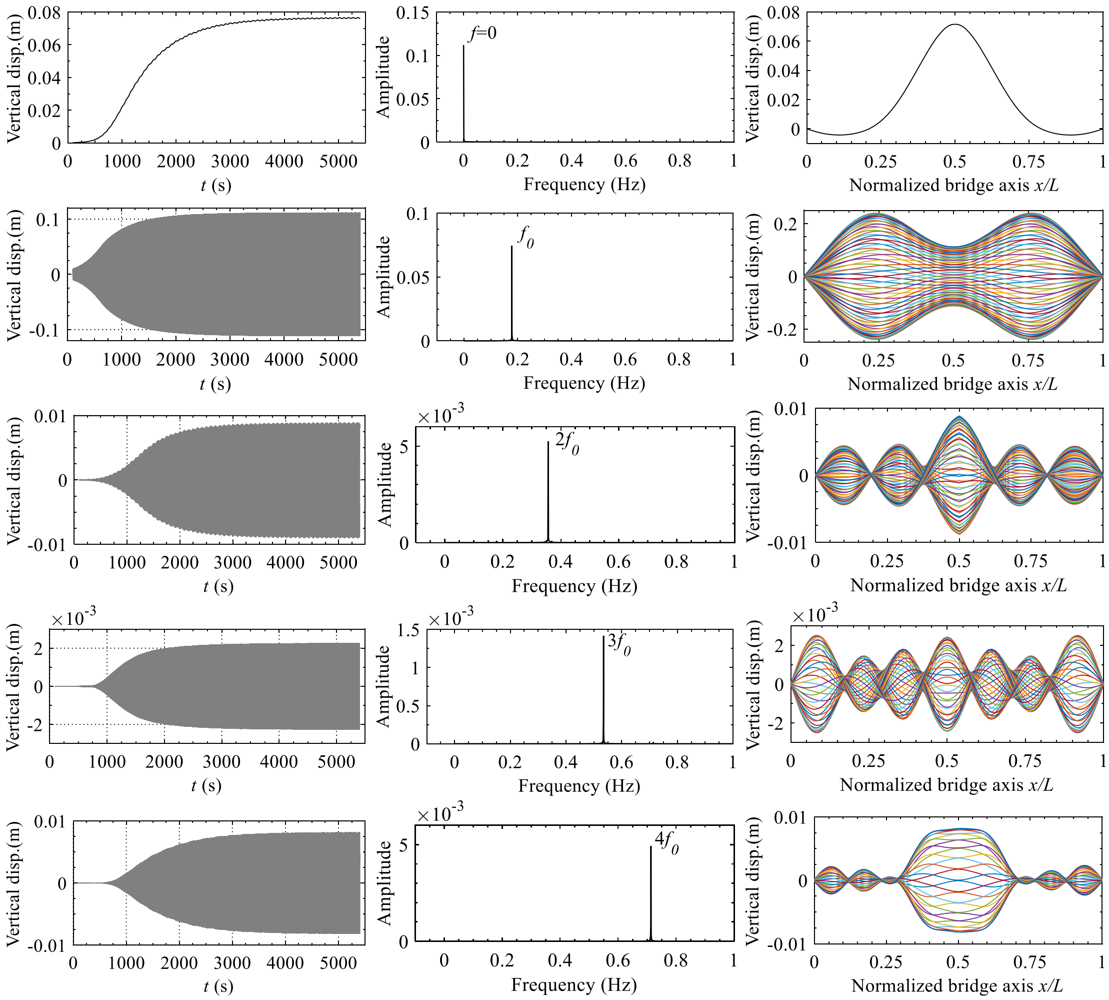

(a)Mid-span displacement component (b) Spectrum of displacement component (c)Vibration shape of displacement component

Fig. 28 Characteristics of vertical displacement components (U = 32 m/s; ξ_s = 0; large deformation effect)

further decomposed according to the frequency components in the response spectra. Figures 27 and 28 display the displacement components corresponding to the frequency components in response spectra at wind speed of 32 m/s. For the torsional displacement, it can be seen that the displacement components with frequencies $3f_0$ and $5f_0$ are almost zero at small vibration amplitude stage but start to increase from zero after the amplitude of displacement component with the fundamental harmonic frequency f_0 reaches about 1.5°. When the displacement component with frequency f_0 gets into a stable vibration stage, so do the other displacement components with higher harmonic frequencies. Hence, it can be concluded that the geometric nonlinear effect should be considered in the nonlinear flutter analysis of this bridge when the amplitude at mid-span reaches about 1.5°. Besides, one can observe that the vibration shape corresponding to fundamental harmonic frequency f_0 is the mode shape T–S-1; the vibration shape corresponding to frequency $3f_0$ is close to the mode shape T–S-3; and the vibration shape corresponding to frequency $5f_0$ is a higher-order torsional mode shape. Another noteworthy aspect is that the stable torsional amplitude at mid-span of the displacement component with frequency $3f_0$ is about 0.35°, accounting for about 6.3% of 5.5° (the stable amplitude of the displacement component with frequency f_0). However, the stable torsional amplitude corresponding to frequency $5f_0$ is a small amount. For the vertical displacement, the vibration

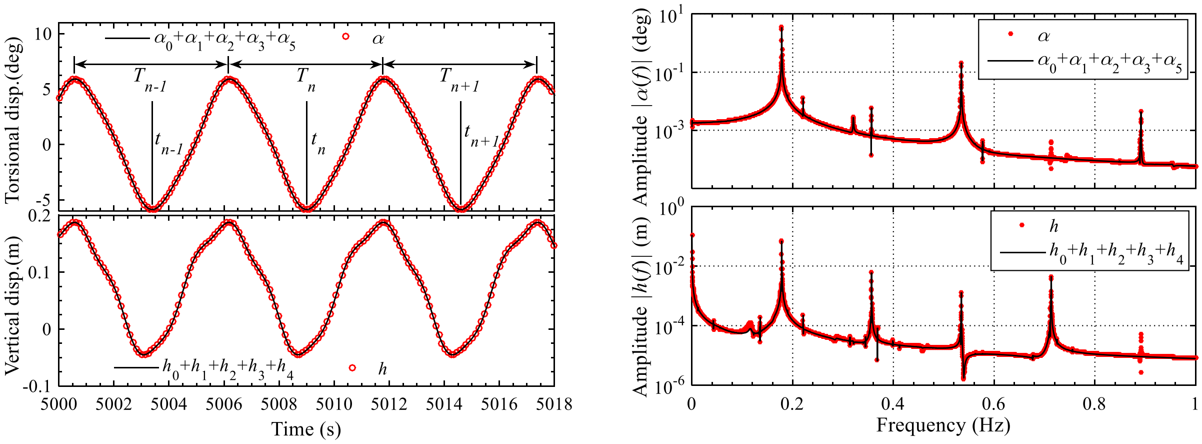

(a) Time histories of displacement responses (b) Spectra of displacement responses

Fig. 29 Comparison of original and reconstructed displacement responses at mid-span (U = 32 m/s, case 4)

shapes corresponding to higher harmonic frequency components are the higher-order vertical mode shapes, which are basically similar to the torsional displacement. Besides, there is a non-oscillatory component with zero frequency (see in the top plots of Fig. 28) in the vertical displacement, which is caused by the geometric nonlinear effect and cannot be predicted by the frequency-domain method.

To further investigate the reasons for the reduction of nonlinear flutter amplitude caused by geometric nonlinearity. Taking U = 32 m/s of case 4 as an example, the work done by aerodynamic forces on each displacement component was calculated separately. According to Figs. 27 and 28, the original torsional displacement α and vertical displacement h can be decomposed as:

$$\alpha \approx \alpha_0 + \alpha_1 + \alpha_2 + \alpha_3 + \alpha_5, \tag{38}$$

$$h \approx h_0 + h_1 + h_2 + h_3 + h_4, \tag{39}$$

in which d_0 ($d = \alpha$ or h) represents the displacement component with frequency 0, d_i ($d = \alpha$ or h; $i = 1,2,3\cdots$) represents the displacement component with frequency if_0. It can be seen from Fig. 29 that the time histories and spectra of original displacement responses all can be well reconstructed by the sum of all displacement components shown in Figs. 27 and 28. As shown in Fig. 29, T_n represents one vibration period of the original torsional displacement at mid-span and t_n represents the position of T_n in the dimension of time. The works $W_{\alpha i}$ and W_{hi} ($i = 1,2,3\cdots$) done by aerodynamic forces on all displacement components of all nodes within one vibration period T_n are calculated. The specific calculation formulas are given as follows:

$$W_{\alpha i} = \int_0^L \int_t^{t+T_n} M_{\text{se,non}}(x)\dot{\alpha}_i(x)\mathrm{d}t\mathrm{d}x, \quad (i = 1,2,3\cdots), \tag{40}$$

$$W_{hi} = \int_0^L \int_t^{t+T_n} L_{\text{se,non}}(x)\dot{h}_i(x)\mathrm{d}t\mathrm{d}x, \quad (i = 1,2,3\cdots), \tag{41}$$

in which L represents the length of the bridge deck. The evolution of works done by aerodynamic forces on all displacement components within one period T_n with time t_n is given in Fig. 30. One can found that the airflow always does positive work on α_1 and h_1 at the stable amplitude stage (i.e., the wind inputs energy to the fundamental harmonic vibration). On the other hand, the airflow always does negative work on α_2, α_3, α_5, h_2, h_3 and h_4 at the stable amplitude stage (i.e., the energy of super-harmonic vibrations is dissipated by the wind). Moreover, it can be found that the energy is mainly dissipated through the third super-harmonic torsional vibration (i.e., α_3).

For a better understanding, the following simple explanation is provided. As shown in Figs. 15, 27, 28, and 31 (the fundamental harmonic frequency f_0 is given for cases 3 and 4 in Fig. 31), the frequency and vibration shape of fundamental harmonic vibration of case 4 are basically consistent with that of case 1, so

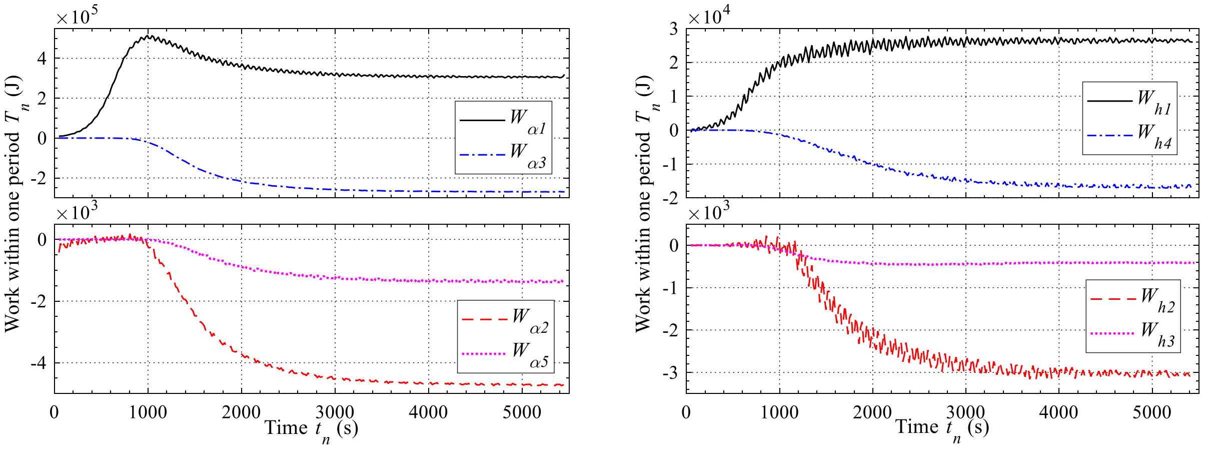

(a) Torsional displacement components

(b) Vertical displacement components

Fig. 30 The evolution of works done by aerodynamic forces within one period T_n with time t_n (U = 32 m/s, case 4)

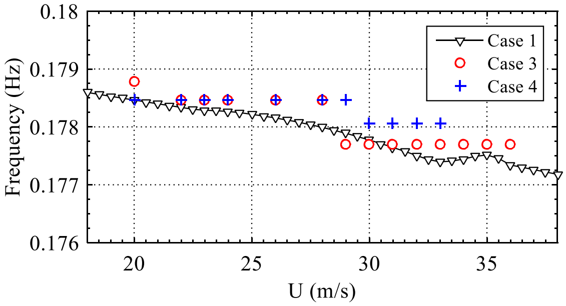

Fig. 31 Frequency of nonlinear flutter for cases 1, 3 and 4

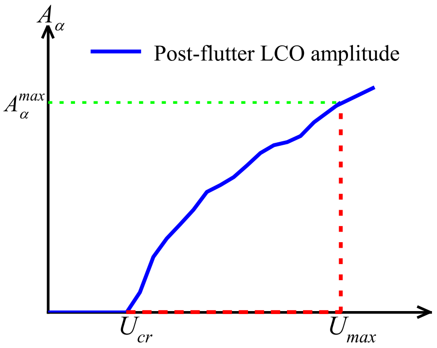

Fig. 32 Schematic diagram for typical nonlinear flutter responses

that the evolution of fundamental harmonic vibration of case 4 should be basically consistent with case 1. However, as shown in Figs. 14 and 27, the stable amplitude of case 4 is only about 5.6°, which is smaller than that of case 1 (i.e., 8.8°), so that the wind is constantly inputting energy into the fundamental harmonic vibration at stable amplitude of 5.6° because its aerodynamic damping is still negative. For the super-harmonic vibrations, their aerodynamic damping is positive since the reduced wind speed (*U*/*bf*) of them is much less than that of the fundamental harmonic vibration, so that the energy of them is dissipated by the wind. Besides, since the super-harmonic vibrations are induced by structural geometric nonlinearity, the energy caused super-harmonic vibrations must have come from the structure itself (i.e., the preexisting fundamental harmonic vibration). As such, the super-harmonic vibrations are equivalent to adding a positive structural damping effect to the fundamental harmonic vibration, which thus causes a reduction in the amplitude of post-flutter and stabilized at 5.6°.

According to the above analysis, the geometric nonlinear effect will become more and more significant with the increase of vibration amplitude and thus will induce a super-harmonic resonance behavior. This behavior is mainly characterized by the higher harmonic frequencies vibrations with higher-order mode shapes involved in the vertical and torsional displacement responses. In addition, the greater the amplitude, the more significant the super-harmonic resonance behavior. The energies of the vibrations with higher harmonic frequencies (i.e., the super-harmonic vibrations) originate from the preexisting vibration with fundamental harmonic frequency (i.e., the fundamental harmonic vibration). However, the

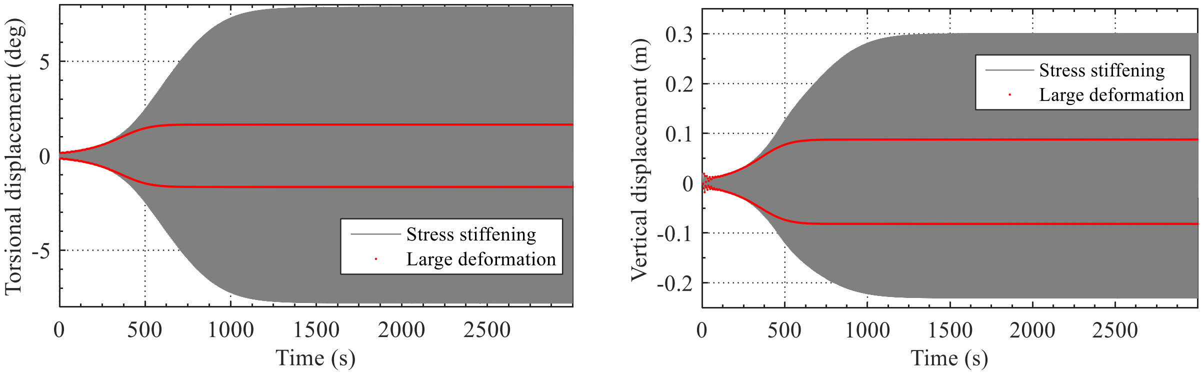

(a) Torsional displacement (b) Vertical displacement

Fig. 33 Time histories of displacements at mid-span of case 5 and case 6 (U = 42 m/s; ξ_s = 0.3%)

absorbed energies of super-harmonic vibrations will be continuously dissipated by the airflow since the aerodynamic damping of the vibrations with higher harmonic frequencies is positive due to their lower reduced wind speed. Consequently, the super-harmonic vibrations play a role of absorbing energy and reducing vibration (similar to tuned mass damper effect) for the fundamental harmonic vibration, which is the main physical mechanism for the reduction in the amplitude of post-flutter response (dominated by the fundamental harmonic vibration) after the geometric nonlinear effect is considered. Besides, it is worth noting that the similar super-harmonic vibration phenomenon was also reported recently in a numerical simulation study on the 3D full-bridge flutter of Tacoma Narrows Bridge [58] (both aerodynamic and geometric nonlinearities were considered), as well as a wind tunnel test study on the large amplitude flutter of a full-bridge aeroelastic model [59].

As mentioned in Introduction, the future performance-based fortification criteria against nonlinear flutter will focus on the acceptable maximum amplitude A_{α}^{max} of post-flutter LCO rather than the critical wind speed U_{cr} [29, 34, 36, 37], as shown in Fig. 32. Generally speaking, the determination of acceptable maximum amplitude A_{α}^{max} for a specific bridge relies on the accurate estimation of displacement, acceleration and stress responses during post-flutter LCO. Therefore, on the one hand, since both the structural and aerodynamic nonlinear effects can be taken into account simultaneously by the developed nonlinear numerical scheme in this study, the more accurate post-flutter responses of bridges can be obtained, which is the foundation for establishing the above performance-based fortification criteria against flutter; on the other hand, it can be seen from the above analysis that the large deformation effect has a significant impact on the stable amplitudes and 3D vibration shape of nonlinear flutter, which indicates that the large deformation effect should be taken into account during the nonlinear flutter analysis of bridges and the determination of A_{α}^{max} in the future performance-based fortification criteria. Meanwhile, since the large deformation effect can significantly reduce the amplitude of post-flutter, the more wind-resistant potentialities can be exploited and thus also encouraged the confidence in the establishment of the performance-based fortification criteria against flutter in the future.

Additionally, the above analysis results still need further verification from wind tunnel tests of a three-dimensional full-bridge aeroelastic model. However, this verification work is very challenging at present, because how to accurately simulate the geometric nonlinearity of real bridges in aeroelastic model and how to identify and quantify other complex nonlinear damping behaviors in aeroelastic model are still very difficult works so far.

5.4.2 *Cases with structural damping*

To validate that the above-mentioned super-harmonic resonance behavior induced by geometric nonlinearity is not a special behavior existing in the undamped structure, investigating the response characteristics of the damped structure is necessary. To this end,

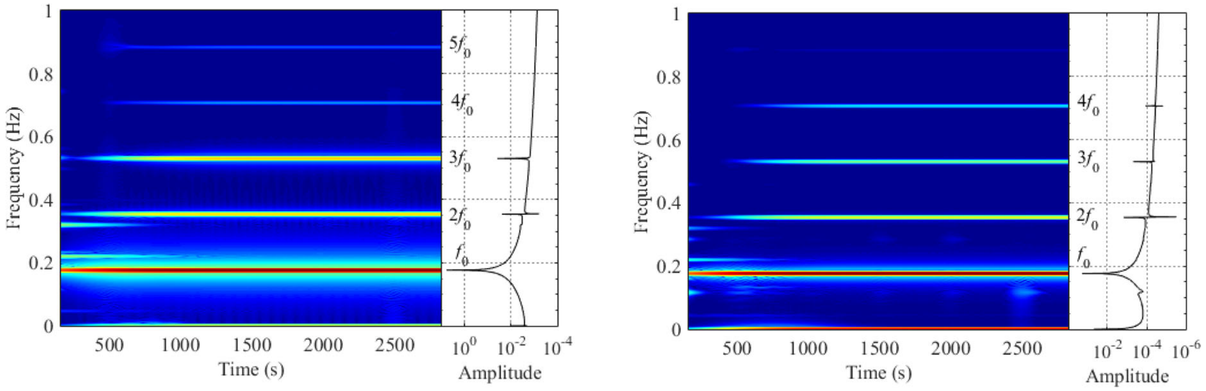

(a) Torsional displacement (b) Vertical displacement

Fig. 34 Time–frequency spectra of the corresponding responses considering stress stiffening effect in Fig. 33 (U = 42 m/s; ξ_s = 0.3%)

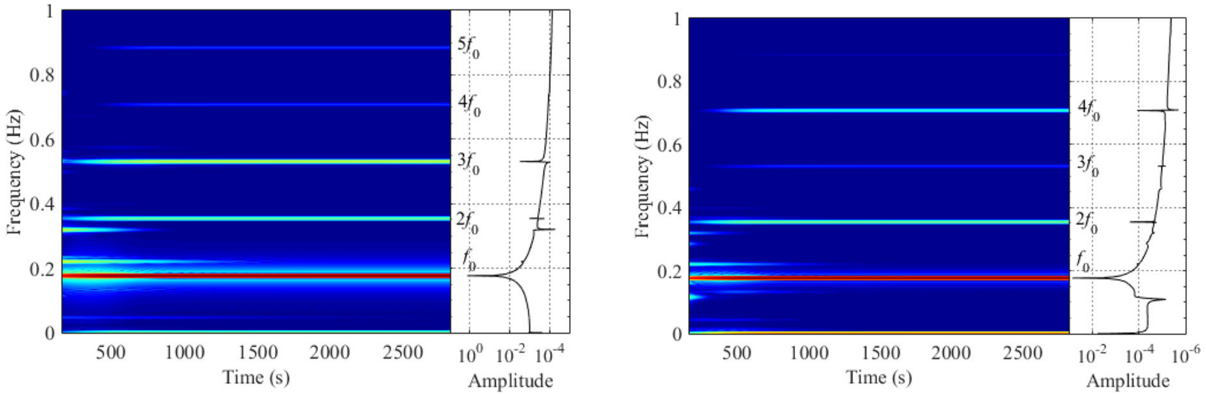

(a) Torsional displacement (b) Vertical displacement

Fig. 35 Time–frequency spectra of the corresponding responses considering large deformation effect in Fig. 33 (U = 42 m/s; ξ_s = 0.3%)

Figs. 33, 34, and 35 show the displacement responses and the corresponding time–frequency spectra when ξ_s = 0.3% and U = 42 m/s. It can be found that even if the stable amplitude considering large deformation effect is small (the torsional stable amplitude is about 1.7°), very weak higher harmonic frequency components in the response can still be observed, which indicates that there is a weak super-harmonic resonance behavior. In addition, it should be noted that the large reduction of amplitude after considering the large deformation effect is mainly caused by the increase of Rayleigh damping due to the geometric nonlinear effect, as shown in Fig. 17b, but has little to do with the weak super-harmonic resonance.

6 Conclusions

In this study, a full-mode coupled nonlinear flutter analysis method and a nonlinear numerical scheme integrating a 3D nonlinear finite element model (considering geometric nonlinearity) and a time-dependent nonlinear self-excited force model (considering aerodynamic nonlinearity) were developed to investigate the influence of geometric nonlinearity on post-flutter responses. The major conclusions are as follows:

(1) The proposed time-dependent nonlinear self-excited forces model can well describe the nonlinear and unsteady characteristics of the

self-excited force under large amplitude vibrations. The model can be combined with nonlinear finite element model to simulate the whole evolution process of 3D post-flutter under the coupling effect of structural and aerodynamic nonlinearities.

(2) The geometric nonlinear effect will become more and more significant with the increase of vibration amplitude and thus will induce a super-harmonic resonance behavior. This behavior is mainly characterized by the higher harmonic frequencies vibrations with higher-order mode shapes involved in the vertical and torsional displacement responses; and the larger the amplitude, the more significant the super-harmonic resonance behavior. Besides, the geometric nonlinear effect will also cause a significant uplifting of the bridge deck in the vertical direction during 3D nonlinear flutter process.

(3) The energies of the vibrations with higher harmonic frequencies (i.e., the super-harmonic vibrations) originate from the preexisting vibration with fundamental harmonic frequency (i.e., the fundamental harmonic vibration). However, the absorbed energies of super-harmonic vibrations will be continuously dissipated by the airflow since the aerodynamic damping of the vibrations with higher harmonic frequencies is positive due to their lower reduced wind speed. Consequently, the super-harmonic vibrations play a role of absorbing energy and reducing vibration (similar to tuned mass damper effect) for the fundamental harmonic vibration, which is the main physical mechanism for the reduction in the amplitude of post-flutter response (dominated by the fundamental harmonic vibration) after the geometric nonlinear effect is considered.

(4) The geometric nonlinear behaviors, such as stress stiffening effect and large deformation effect, cannot be ignored in the 3D nonlinear flutter analysis of long-span suspension bridges. Otherwise, the post-flutter responses may be overestimated. The large deformation effect can induce a more significant super-harmonic resonance behavior compared with only considering the stress stiffening effect and thus further reduce the amplitude of post-flutter more significantly. For the long-span suspension bridge studied in this paper, a weak super-harmonic resonance behavior starts to appear when the torsional amplitude at mid-span is only greater than 1.5°, which means that the geometric nonlinear effect may be worth considering at this time.

In view of the shortcoming of Rayleigh damping model in 3D nonlinear flutter analysis, a nonlinear structural damping model suitable for real bridges should be developed in future work, and the damaging stress level of critical components of long-span bridges during the post-flutter should be further investigated. Besides, the symbol calculation method based on neural networks proposed by Zhang et al. [60–63] recently opens up a general symbolic computing path for the analytic solution of nonlinear partial differential equation, which may also be used for the analytic solution of the nonlinear wind-bridge coupled system described in this study in the future work.

Acknowledgements This work described in this paper is supported by the National Natural Science Fund of China (No. 52308480; 52178451; 52178450; 52178452). The authors would also like to gratefully acknowledge the support from the Open Fund of Key Laboratory of Bridge Engineering Safety Control by Department of Education (Changsha University of Science & Technology) (No.12KB01).

Author contributions KL involved in conceptualization, methodology, formal analysis, investigation, funding acquisition, and writing—original draft. YH involved in conceptualization, methodology, funding acquisition, supervision and writing-review & editing. CSC involved in methodology, investigation, and writing—review and editing. WZ involved in writing—review and editing. JS involved in validation and visualization. HY involved in validation and visualization.

Funding The authors have not disclosed any funding.

Availability of data and material All data generated or analyzed during this study are included in this article.

Declarations

Conflict of interest The authors declare that they have no known competing financial interests or personal relationships that could have appeared to influence the work reported in this paper.

References

1. Chen, X., Kareem, A.: Revisiting multimode coupled bridge flutter: some new insights. J. Eng. Mech. **132**(10), 1115–1123 (2006)
2. Chen, X.: Improved understanding of bimodal coupled bridge flutter based on closed-form solutions. J. Struct. Eng. **133**(1), 22–31 (2007)
3. Matsumoto, M.: Aerodynamic damping of prisms. J. Wind Eng. Ind. Aerodyn. **59**, 159–175 (1996)
4. Matsumoto, M., Daito, Y., Yoshizumi, F., Ichikawa, Y., Yabutani, T.: Torsional flutter of bluff bodies. J. Wind Eng. Ind. Aerod. **69**, 871–882 (1997)
5. Matsumoto, M., Kobayashi, Y., Shirato, H.: The influence of aerodynamic derivatives on flutter. J. Wind Eng. Ind. Aerodyn. **60**, 227–239 (1996)
6. Yang, Y., Wu, T., Ge, Y., Kareem, A.: Aerodynamic stabilization mechanism of a twin box girder with various slot widths. J. Bridge Eng. **20**(3), 04014067 (2015)
7. Agar, T.: The analysis of aerodynamic flutter of suspension bridges. J. Comput. Struct. **30**(3), 593–600 (1988)
8. Agar, T.: Aerodynamic flutter analysis of suspension bridges by a modal technique. J. Eng. Struct. **11**, 75–82 (1989)
9. Namini, A., Albrecht, P., Bosch, H.: Finite element based flutter analysis of cable suspended bridges. J. Struct. Eng. **118**(6), 1509–1526 (1992)
10. Jain, A., Jones, N., Scanlan, R.: Coupled flutter and buffeting analysis of long span bridges. J. Struct. Eng. **122**(7), 716–725 (1996)
11. Chen, X., Matsumoto, M., Kareem, A.: Aerodynamic coupling effects of flutter and buffeting of bridges. J. Eng. Mech. **126**(1), 17–26 (2000)
12. Ge, Y.J., Tanaka, H.: Aerodynamic flutter analysis of cable-supported bridges by multi-mode and full-mode approaches. J. Wind Eng. Ind. Aerodyn. **86**(2), 123–153 (2000)
13. Hua, X.G., Chen, Z.Q.: Full-order and multimode flutter analysis using ANSYS. Finite Elem. Anal. Des. **44**(9–10), 537–551 (2008)
14. Scanlan, R.H., Tomko, J.: Airfoil and bridge deck flutter derivatives. J. Soil Mech. Found. Div. **97**(6), 1717–1737 (1971)
15. Scanlan, R.: Amplitude and turbulence effects on bridge flutter derivatives. J. Struct. Eng. **123**(2), 232–236 (1997)
16. Noda, M., Utsunomiya, H., Nagao, F., Kanda, M., Shiraishi, N.: Effects of oscillation amplitude on aerodynamic derivatives. J. Wind Eng. Ind. Aerodyn. **91**, 101–111 (2003)
17. Chen, Z.Q., Yu, X.D., Yang, G., Spencer, B.F., Jr.: Wind-induced self-excited loads on bridges. J. Struct. Eng. **131**(12), 1783–1793 (2005)
18. Mannini, C., Sbragi, G., Schewe, G.: Analysis of self-excited forces for a box-girder bridge deck through unsteady RANS simulations. J. Fluids Struct. **63**, 57–76 (2016)
19. Xu, F., Ying, X., Zhang, Z.: Effects of exponentially modified sinusoidal oscillation and amplitude on bridge deck flutter derivatives. J. Bridge Eng. **21**(5), 06016001 (2016)
20. Matsumoto, M., Shirato, H., Hirai, S.: Torsional flutter mechanism of 2-D H-shaped cylinders and effect of flow turbulence. J. Wind Eng. Ind. Aerod. **41**(1–3), 687–698 (1992)
21. Daito, Y., Matsumoto, M., Araki, K.: Torsional flutter mechanism of two-edge girders for long-span cable-stayed bridge. J. Wind Eng. Ind. Aerod. **90**, 2127–2141 (2002)
22. Gao, G.Z., Zhu, L.D., Han, W.S., Li, J.W.: Nonlinear post-flutter behavior and self-excited force model of a twin-side-girder bridge deck. J. Wind Eng. Ind. Aerod. **177**, 227–241 (2018)
23. Tang, Y., Hua, X.G., Chen, Z.Q., Zhou, Y.: Experimental investigation of flutter characteristics of shallow π section at post-critical regime. J. Fluid Struct. **88**, 275–291 (2019)
24. Michelin, S., Choquel Amandolese, M.: Low speed flutter and limit cycle oscillations of a two-degree-of-freedom flat plate in a wind tunnel. J. Fluid Struct. **43**, 244–255 (2013)
25. Pigolotti, L., Mannini, C., Bartoli, G.: Experimental study on the flutter-induced motion of two-degree-of-freedom plates. J. Fluid Struct. **75**, 77–98 (2017)
26. Gao, G.Z., Zhu, L.D., Wang, F., Bai, H., Hao, J.M.: Experimental investigation on the nonlinear coupled flutter motion of a typical flat closed-box bridge deck. J. Sens. Basel. **20**(2), 568 (2020)
27. Xu, F., Yang, J., Zhang, M., Yu, H.: Experimental investigations on post-flutter performance of a bridge deck sectional model using a novel testing device. J. Wind Eng. Ind. Aerod. **217**, 104752 (2021)
28. Wu, B., Chen, X.Z., Wang, Q., Liao, H.L., Dong, J.H.: Characterization of vibration amplitude of nonlinear bridge flutter from sectional model test to full bridge estimation. J. Wind Eng. Ind. Aerod. **197**, 104048 (2020)
29. Li, K., Han, Y., Cai, C.S., Hu, P., Li, C.: Experimental investigation on post-flutter characteristics of a typical steel-truss suspension bridge deck. J. Wind Eng. Ind. Aerodyn. **216**, 104724 (2021)
30. Wu, B., Wang, Q., Liao, H., Mei, H.: Hysteresis response of nonlinear flutter of a truss girder: experimental investigations and theoretical predictions. J. Comput. Struct. **238**, 106267 (2020)
31. Yuan, W., Laima, S., Chen, W.L., Li, H.: External excitation effects on the flutter characteristics of a 2-DOF rigid rectangular panel. J. Wind Eng. Ind. Aerod. **209**, 104486 (2021)
32. Zhang, M., Xu, F., Ying, X.: Experimental Investigations on the nonlinear torsional flutter of a bridge deck. J. Bridge Eng. **22**(8), 04017048 (2017)
33. Gao, G., Zhu, L., Li, J., Han, W., Yao, B.: A novel two-degree-of-freedom model of nonlinear self-excited force for coupled flutter instability of bridge decks. J. Sound Vib. **480**, 115406 (2020)
34. Li Kai.: Nonlinear Flutter Characteristics of Long-Span Bridges and Its Analytical Method. Doctoral Thesis, Changsha University of Science and Technology, China (2022). (In Chinese)
35. Wang, Y., Chen, X., Li, Y.: Nonlinear self-excited forces and aerodynamic damping associated with vortex induced vibration and flutter of long span bridge. J. Wind Eng. Ind. Aerodyn. **204**, 104207 (2020)
36. Zhu, L.D., Gao, G.Z., Zhu, Q.: Recent advances, future application and challenges in nonlinear flutter theory of long span bridges. J. Wind Eng. Ind. Aerodyn. **206**, 104307 (2020)

37. Zhang, M., Xu, F., Wu, T., Zhang, Z.B.: Post flutter analysis of bridge decks using aerodynamic describing functions. J. Bridge Eng. **25**(8), 04020046 (2020)
38. Zhang, Z.T.: Multistage indicial functions and post flutter simulation of long-span bridges. J. Bridge Eng. **23**(4), 04018010 (2018)
39. Wu, T., Kareem, A.: A nonlinear convolution scheme to simulate bridge aerodynamics. Comput. Struct. J. **128**, 259–271 (2013)
40. Wu, T., Kareem, A., Ge, Y.J.: Bridge aerodynamics and aeroelasticity: a comparison of modeling schemes linear and nonlinear aeroelastic analysis frameworks for cable-supported bridges. J. Nonlinear Dyn. **74**, 487–516 (2013)
41. Liu SY.: Nonlinear Aerodynamic Model and Non-stationary Whole Process Wind Response of Long Span Bridges. Doctoral Thesis, Tongji University, China (2014) (In Chinese).
42. Zhou, R., Yang, Y.X., Ge, Y.J., Du, Y.L., Zhang, L.H.: Wind-induced nonlinear behaviors of twin-box girder bridges with various aerodynamic shapes. J. Nonlinear Dyn. **6**, 1–21 (2018)
43. Li, W., Laima, S., Jin, X., Yuan, W., Li, H.: A novel long short-term memory neural-network-based self-excited force model of limit cycle oscillations of nonlinear flutter for various aerodynamic configurations. J. Nonlinear Dyn. **100**(3), 2071–2087 (2020)
44. Zhang, R., Bilige, S., Chaolu, T.: Fractal solitons, arbitrary function solutions, exact periodic wave and breathers for a nonlinear partial differential equation by using bilinear neural network method. J. Syst. Sci. Complex. **34**, 122–139 (2021)
45. Li, K., Kou, J., Zhang, W.: Deep neural network for unsteady aerodynamic and aeroelastic modeling across multiple Mach numbers. J. Nonlinear Dyn. **96**(3), 2157–2177 (2019)
46. Li, T., Wu, T., Liu, Z.: Nonlinear unsteady bridge aerodynamics: reduced-order modeling based on deep LSTM networks. J. Wind Eng. Ind. Aerodyn. **198**, 104116 (2020)
47. Zhang, R.F., Li, M.C., Yin, H.M.: Rogue wave solutions and the bright and dark solitons of the (3+1)-dimensional Jimbo–Miwa equation. Nonlinear Dyn. **103**, 1071–1079 (2021)
48. Zhang, R.F., Bilige, S.: Bilinear neural network method to obtain the exact analytical solutions of nonlinear partial differential equations and its application to p-gBKP equation. Nonlinear Dyn. **95**, 3041–3048 (2019)
49. Li, K., Han, Y., Song, J., Cai, C.S., Hu, P., Qiu, Z.X.: Three-dimensional nonlinear flutter analysis of long-span bridges by multimode and full-mode approaches. J. Wind Eng. Ind. Aerodyn. **242**, 105554 (2023)
50. Clough, R.W., Penzien, J.: Dynamics of Structures, 2nd edn. McGraw-Hill, New York (1993)
51. Lin, Y.K., Yang, J.N.: Multimode bridge response to wind excitations. J. Eng. Mech. **109**(2), 586–603 (1983)
52. Chen, X., Matsumoto, M., Kareem, A.: Time domain flutter and buffeting response analysis of bridges. J. Eng. Mech. **126**(1), 7–16 (2000)
53. Chen, X., Kareem, A., Matsumoto, M.: Multimode coupled flutter and buffeting analysis of long span bridges. J. Wind Eng. Ind. Aerodyn. **89**(7), 649–664 (2001)
54. Han, Y., Li, K., Cai, C.S.: Study of central buckle effects on flutter of long-span suspension bridges. Wind Struct. Int. J. **35**(5), 000 (2020)
55. Rooij, A.C.L.M.V., Nitzsche, J., Dwight, R.P.: Energy budget analysis of aeroelastic limit-cycle oscillations. J. Fluids Struct. **69**, 174–186 (2017)
56. Zhang, M., Xu, F., Zhang, Z., Ying, X.: Energy budget analysis and engineering modeling of post-flutter limit cycle oscillation of a bridge deck. J. Wind Eng. Ind. Aerodyn. **188**, 410–420 (2019)
57. Mashnad, M., Jones, N.P.: A model for vortex-induced vibration analysis of long-span bridges. J. Wind Eng. Ind. Aerodyn. **134**, 96–108 (2014)
58. Song, D., Kim, W., Kwon, O.K., et al.: Vertical and torsional vibrations before the collapse of the Tacoma narrows bridge in 1940. J. Fluid Mech. **949**, A11 (2022)
59. Zhang, Z., Wang, Z., Zeng, J., et al.: Experimental investigation of post-flutter properties of a suspension bridge with a π-shaped deck section. J. Fluids Struct. **112**, 103592 (2022)
60. Zhang, R.F., Li, M.C., Cherraf, A., et al.: The interference wave and the bright and dark soliton for two integro-differential equation by using BNNM. Nonlinear Dyn. **111**, 8637–8646 (2023)
61. Zhang, R.F., Bilige, S., Liu, J.-G., Li, M.: Bright-dark solitons and interaction phenomenon for p-gBKP equation by using bilinear neural network method. Phys. Scr. **96**, 025224 (2021)
62. Zhang, R.F., Li, M.C., Gan, J.Y., et al.: Novel trial functions and rogue waves of generalized breaking soliton equation via bilinear neural network method. Chaos Solitons Fractals **154**, 111692 (2022)
63. Zhang, R.F., Li, M.C., Albishari, M.: Generalized lump solutions, classical lump solutions and rogue waves of the (2+1)-dimensional Caudrey–Dodd–Gibbon–Kotera–Sawada-like equation. Appl. Math. Comput. **403**, 126201 (2021)